Improvements to the Range Stack Straw Chambers for the Measurement of $K^+ \rightarrow \pi^+ \nu\bar{\nu}$

by

XINGHUA LI

B.Sc., Shandong University (China), 1996

A THESIS SUBMITTED IN PARTIAL FULFILMENT OF THE REQUIREMENTS FOR THE DEGREE OF

Master of Science

in

The Faculty of Graduate Studies

Department of Physics and Astronomy

We accept this thesis as conforming to the required standard

The University of British Columbia

April 2002

Abstract

Experiments E787/E949 at Brookhaven National Lab are aiming to measure the rare decay $K^+ \to \pi^+\nu\bar{\nu}$, expected in the Standard Model to have a branching ratio on the order of 10^{-10}. This thesis is related to improvements to the performance of one of the subsystems – the Range Stack Straw Chambers (RSSCs) which are designed to assist in the charged particle tracking and range measurements. There was a long-standing problem of poor resolution in the RSSCs longitudinal (z) measurement. In this thesis, we focus on understanding the sources of the problem and testing of a solution – a new electronics front end amplifier board developed by the TRIUMF electronics group. The new electronics uses two discriminator thresholds: the high threshold serves to remove cross talk effects and the low threshold serves to reduce time walk effects, resulting in improved resolution. Bench tests of the new system at TRIUMF from 1999 - 2001 showed significantly improved z resolution. A factor of 2 improvement was obtained, giving a z resolution of 1.5 cm. Initial results from E949 cosmic ray and muon data show a substantial z measurement improvement.

Table of Contents

List of Tables

List of Figures

Acknowledgments

When I decided to pursue a Masters Degree abroad, I had no any idea what the other country looks like – the life style, the communication, the culture and the education. When I started looking for my major field, Janis McKenna informed me there is a particle physics group in TRIUMF which is cooperating with BNL with a research on rare kaon decay. It sounded interesting and challenging for me. I came to TRIUMF and started my master study here.

I would like to thank Shaomin Chen who played an important role in my Master study. Many thanks to Toshio Numao, Joe Mildenberger, Jingliang Hu, Akira Konaka, Renee Poutissou, Paul Bergbusch who also gave me so much help in my work. And I'd like to thank Miles Constable, Ray Bula, Chapman Lim and John Cresswell for working on RSSC design, adjustment and repair without whose effort this thesis would not be a reality. Finally, I would like to thank Doug Bryman, my M.Sc. supervisor, for his guidance , co-working on RSSC bench testing, insight in helping me to complete a Masters degree.

Introduction

The experiment E787 at Brookhaven National Laboratory discovered the important rare kaon decay, $K^+ \to \pi^+\nu\bar{\nu}$ with the observation of two candidate events with a background level of 0.15 events estimated[1]. E949, the successor to E787, will run with higher kaon fluxes and will increase the single event sensitivity by an order of magnitude taking advantage of a number of upgrades to the E787 detector. Modification to the electronic readout of tracking chambers studied in this thesis is one aspect of the upgrade designed to improve the performance of the experiment.

1.1 Theory

1.1.1 The Standard Model

The Standard Model (SM) of Particle Physics, which provides a consistent theoretical picture of our world's fundamental elementary particles and interactions among them, still contains many not fully understood parameters. These parameters such as those in the Cabibbo-Kobayashi-Maskawa (CKM) matrix are not predicated by theory. Precise measurement of these parameters can either confirm the SM or indicate new physics beyond the SM.

In the SM, present evidence indicates that matter is built from two types of fundamental fermions, quarks and leptons, which are structureless and pointlike on the scale of 10^{-17} m. There are three generations of leptons and quarks. Interactions among quarks of different charge are described by a so-called CKM matrix.

$$\begin{pmatrix} d' \\ s' \\ b' \end{pmatrix} = \begin{pmatrix} V_{ud} & V_{us} & V_{ub} \\ V_{cd} & V_{cs} & V_{cb} \\ V_{td} & V_{ts} & V_{tb} \end{pmatrix} \begin{pmatrix} d \\ s \\ b \end{pmatrix}. \tag{1.1}$$

The quarks interact with each other via strong, weak, electro-magnetic and gravitational forces. The weak interaction is described by a Lagrangian[2] in which the charged current interactions are mediated by W^+, W^- bosons and the weak neutral current interaction by the Z^0 boson. The CKM matrix has four independent parameters which, in the leading order of the Wolfenstein parameterization[3], are A, λ, ρ and η. In this parameterization, the CKM matrix elements are written in powers of Cabibbo angle, $\lambda = \sin\theta_C \simeq 0.22$, as

$$\begin{pmatrix} V_{ud} & V_{us} & V_{ub} \\ V_{cd} & V_{cs} & V_{cb} \\ V_{td} & V_{ts} & V_{tb} \end{pmatrix} \simeq \begin{pmatrix} 1-\lambda^2/2 & \lambda & A\lambda^3(\rho - i\eta) \\ \lambda & 1-\lambda^2/2 & A\lambda^2 \\ A\lambda^3(1-\rho-i\eta) & -A\lambda^2 & 1 \end{pmatrix}, \tag{1.2}$$

The CKM matrix elements can be related in terms of the "unitarity triangle". The unitarity of V_{CKM} requires that

$$V_{ub}^* V_{ud} + V_{cb}^* V_{cd} + V_{tb}^* V_{td} \simeq 0, \tag{1.3}$$

and

$$\frac{V_{ub}^* V_{ud}}{V_{cb}^* V_{cd}} + 1 + \frac{V_{tb}^* V_{td}}{V_{cb}^* V_{cd}} = 0. \tag{1.4}$$

This cancelation results in the flavor changing neutral currents (FCNCs) being forbidden at the lowest level, known as the GIM mechanism. With the use of Wolfenstein parameters this becomes

$$(-\bar{\rho} - i\bar{\eta}) + 1 + (-1 + \bar{\rho} + i\bar{\eta}) \simeq 0 \tag{1.5}$$

where

$$-\bar{\rho} = \rho(1 - \frac{\lambda^2}{2}), -\bar{\eta} = \eta(1 - \frac{\lambda^2}{2})[2] \tag{1.6}$$

which can be represented by a triangle in the complex plane with vertices A = ($\bar{\rho}$, $\bar{\eta}$), B = (1, 0), and C = (0, 0), as illustrated in Fig. 1.1.

1.1.2 Motivation of searching for $K^+ \rightarrow \pi^+\nu\bar{\nu}$

The motivation of the search for the decay $K^+ \rightarrow \pi^+\nu\bar{\nu}$ stems from the desire to measure the small, imprecisely-determined CKM matrix element $|V_{td}|$, the coupling of top to down quarks in the CKM quark mixing matrix. $|V_{td}|$ can be accurately determined by measuring $K^+ \rightarrow \pi^+\nu\bar{\nu}$ after a correction for a charm quark contribution, which is indicated by the solid line extension to the right of (1, 0) in Fig. 1.1. The AD side can be determined from the $K^+ \rightarrow \pi^+\nu\bar{\nu}$ branching ratio.

Another goal is to search for non-SM physics and to study the generation puzzle[4]. The GIM mechanism forbids the first order weak $K^+ \rightarrow \pi^+\nu\bar{\nu}$ decays due to the unitarity of V_{CKM}[2]. Flavor changing neutral currents (FCNC) can only be realized by second order decays, in which the different masses of the internal u, c, t quarks spoil the GIM cancelation. In particular, the very large t quark mass increases the branching ratio for $K^+ \rightarrow \pi^+\nu\bar{\nu}$. An unexpected kinematic signature for the π^+ or a decay rate in conflict with the SM prediction could indirectly reveal the existence of new weakly interacting particles which would have eluded other investigations. For example, $K^+ \rightarrow \pi^+X^0$ and $K^+ \rightarrow \pi^+X^0X^0$ decay modes may include particles X^0 like axions, familons, hyperphotons, etc.

The ultra-rare decay $K^+ \rightarrow \pi^+\nu\bar{\nu}$ is an attractive candidate for study for the following reasons.

- Nearly the entire known spectrum of quarks, leptons, and bosons must interact in the internal loops. Fig 1.2 shows the possible second order decay modes.

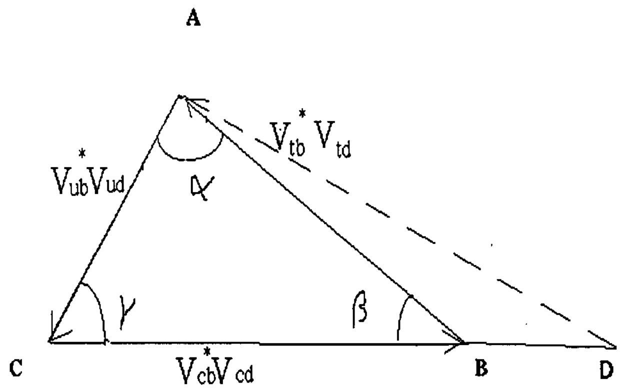

Figure 1.1: *Unitarity triangle in the complex (ρ, η) plane.*

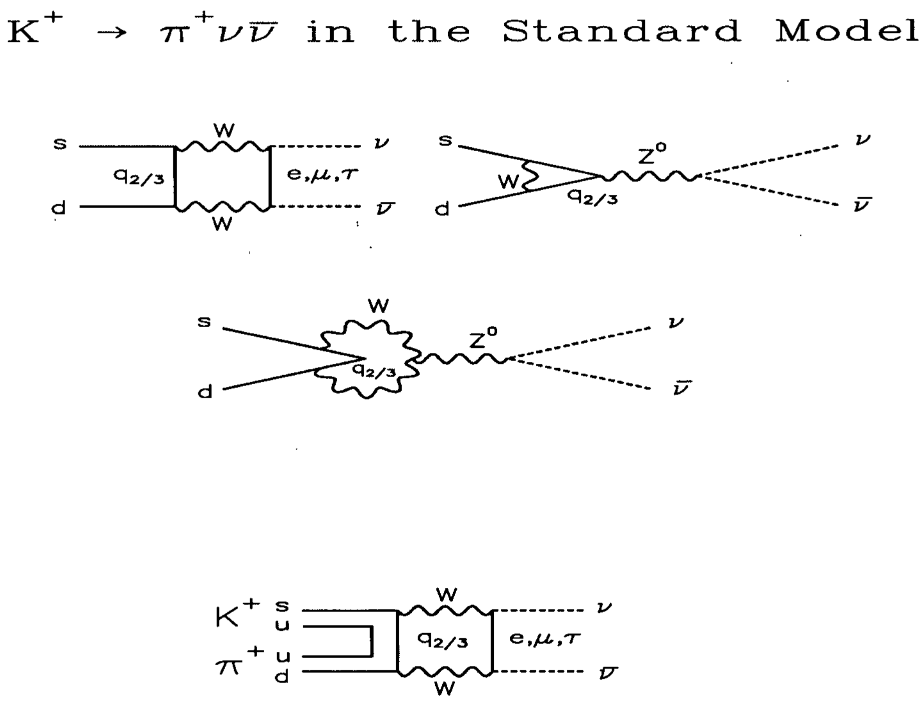

Figure 1.2: *The Feyman diagrams that contribute to the $K^+ \rightarrow \pi^+ \nu \bar{\nu}$ branching ratio. All are second order weak effects.*

- Uncertainties from hadronic effects are removed by normalizing to the branching ratio for the isospin-rotated $K^+ \to \pi^0 e^+ \nu_e$ mode ($B_{K^+ \to \pi^0 e^+ \nu_e} = 0.0482$[5]). The branching ratio can be expressed in simplified form as

$$B(K^+ \to \pi^+ \nu \bar{\nu}) \simeq 4.11 \times 10^{-11} A^4 {X_0}^2(x_t) \frac{1}{\sigma} \Big[(\sigma \bar{\eta})^2 + (\rho_0 - \bar{\rho})^2 \Big]. \tag{1.7}$$

ρ_0 is defined as

$$\rho_0 = 1 + \frac{P_0(X)}{A^2 X_0(x_t)}. \tag{1.8}$$

$\bar{\rho}$, $\bar{\eta}$ and σ are defined by

$$\bar{\rho} = \rho \left(1 - \frac{\lambda^2}{2} \right), \tag{1.9}$$

$$\bar{\eta} = \eta \left(1 - \frac{\lambda^2}{2} \right) \tag{1.10}$$

and

$$\sigma = \left(\frac{1}{1 - \frac{\lambda^2}{2}} \right)^2. \tag{1.11}$$

Equ. (1.7) defines an ellipse in the $(\bar{\rho}, \bar{\eta})$ plane centered at $(\rho_0, 0)$. In the leading order of the Wolfenstein parameterization,

$$\sigma \to 1, \; \bar{\eta} \to \eta, \; \bar{\rho} \to \rho \tag{1.12}$$

and Equ. (1.7) becomes

$$B(K^+ \to \pi^+ \nu \bar{\nu}) = 4.11 \times 10^{-11} A^4 X^2(x_t) \Big[\eta^2 + (\rho_0 - \rho)^2 \Big] \tag{1.13}$$

where

$$X_0(x_t) = \frac{x}{8} \Big[\frac{x+2}{x-1} + \frac{3x - 6}{x-1}^2 lnx \Big], \tag{1.14}$$

$x_t = {m_t}^2 / {m_W}^2$ and ρ_0 represents the charm quark contribution. Typically, ρ_0 is approximately 1.2 - 1.6 [6] which defines a circle in the (ρ, η) plane centered at $(\rho_0, 0)$ with radius r_0 given by

$$r_0^2 = \frac{1}{A^4 X^2(x_t)} \frac{B(K^+ \to \pi^+ \nu\bar{\nu})}{4.11 \times 10^{-11}}. \tag{1.15}$$

- Long distance effects (e.g. those due to internal photon or meson exchange) are negligible down to the 10^{-13}[7] level, in comparison with short distance effects (i.e. those related to quark, lepton and gauge boson exchange).

For the above reasons, $K^+ \to \pi^+\nu\bar{\nu}$ may be the best source of information on the magnitude of the SM parameter $|V_{td}|$. If B($K^+ \to \pi^+\nu\bar{\nu}$), m_t, V_{cb}, etc., were well measured, the precision of $|V_{td}|$ could be determined down to a precision of 6%[9]. QCD corrections to the charm contribution are the leading source of the residual theoretical uncertainty.

1.2 E787 and E949 Experiments

E787 and E949 are kaon stopped experiments. Therefore, the kinematic features of the daughter products are well defined. The signature for $K^+ \to \pi^+\nu\bar{\nu}$ is a K^+ decay to a π^+ of momentum P $<$ 227 MeV/c and no other observable products. Definitive observation of this signal requires suppression of all backgrounds to well below the sensitivity for the signal and reliable estimate of the background levels, preferably to the level of 10^{-11}. The E787 and E949 experiments were designed to achieve this level of sensitivity.

1.2.1 Backgrounds

The most troublesome background sources in the E787 and E949 experiments are:

- $K^+ \to \mu^+\nu_\mu$ decay (called $K_{\mu 2}$) : If the μ^+ is mistaken for a π^+, this event will appear to be $K^+ \to \pi^+\nu\bar{\nu}$. The branching ratio is 64% and the charged track momentum is 236 MeV/c. It is rejected by particle identification, i.e., no $\pi^+ \to \mu^+ \to e^+$ decay chain observed and by its momentum.

- $K^+ \to \pi^+\pi^0$ decay (called $K_{\pi 2}$): If both photons from the π^0 decay are missed, this event looks like $K^+ \to \pi^+\nu\bar{\nu}$. The branching ratio is 21% and the charged track momentum is 205 MeV/c. It is rejected by detecting at least one of the two photons from the π^0 decay and measuring the momentum.

- π^+ scattering events (called π_{scat}) : π^+ from the beam could scatter into the fiducial region of the detector and appear to be $K^+ \to \pi^+\nu\bar{\nu}$ decay. They are rejected by good particle identification in beam counters, tracking of both the kaon and pion, and requiring that the putative kaon decay occurs at rest in the target.

- Charge Exchange: After entering the target, a K^+ can interact with a neutron in a nucleus to produce a K^0 and a proton. The subsequent decay $K^0 \to \pi^+ l^- \bar{\nu}$, where $l = e$ or μ, can mimic $K^+ \to \pi^+\nu\bar{\nu}$ if the lepton is lost. This is called the charge exchange background (CEX). CEX events are cut by looking for a gap between the K^+ and π^+ and by finding the lepton product.

A plot of the momentum spectra of K^+ decay modes is shown in Fig. 1.3. The $K_{\mu 2}$ and $K_{\pi 2}$ decay modes are two-body decays with mono-energetic peaks in their momenta, ranges and kinetic energies. Our target searching mode is three-body decay, which has a continuous momentum spectrum. This figure also depicts many other decay modes, such as $\pi^+\pi^+\pi^-$, $\pi^+\pi^0\pi^0$, $\pi^0\mu^+\nu_\mu$, $\mu^+\nu_\mu\gamma$ which are easier to reject than $K_{\mu 2}$ and $K_{\pi 2}$ due to their low charged-track momenta and/or extra decay products.

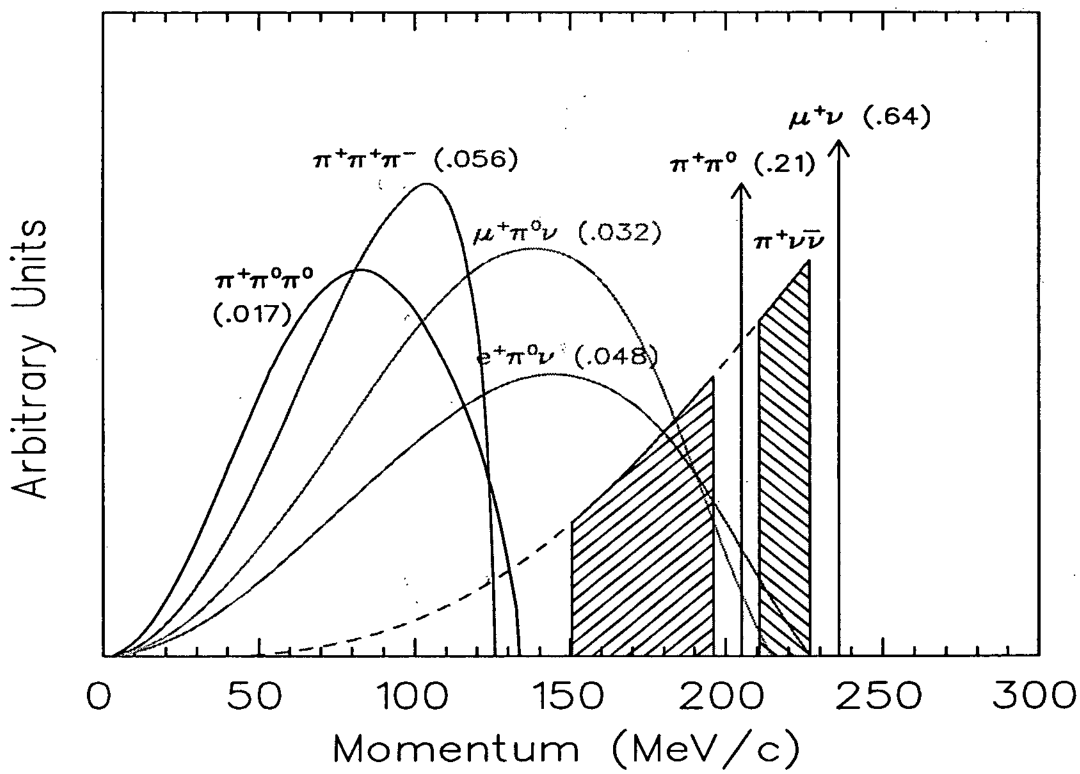

Figure 1.3: *Top seven K^+ decay modes.*

To aid in background suppression, the search takes place away from the $K_{\mu 2}$ and the $K_{\pi 2}$ peaks. E787 and E949 have studied the region above the $K_{\pi 2}$ peak, where little background from these principal decay modes occur. The search was restricted to the measured momentum 211 MeV/c < P < 230 MeV/c between the $K_{\pi 2}$ and $K_{\mu 2}$ peaks, with the maximum pion momentum 227 MeV/c from $K^+ \to \pi^+ \nu \bar{\nu}$ decay at rest[1].

This experiment requires kaons to stop in the center of the detector and decay at rest, making range, energy, and momentum all useful. By using range information, the effective separation between the $K^+ \to \mu^+ \nu_\mu$ and $K^+ \to \pi^+ \pi^0$ is increased due to the fact that muons are more penetrating than pions. However, nuclear reactions complicate the situation. For example, beam pions can interact with material and scatter into the fiducial volume, mimicking the $K^+ \to \pi^+ \nu \bar{\nu}$. In addition, multiple scattering of daughter μ^+ or π^+ from kaon decay can add tails to kinematic measurements. These considerations lead to a set of detector design considerations, such as a low energy, intense pure K^+ beam which can be stopped with a minimum of material, a very good beam pion detection efficiency, very good π^+/μ^+ separation, an active highly segmented K^+ stopping target for clean K^+ and π^+ tracking, redundant measurements of the π^+ momentum and a redundant μ^+ veto system as well as hermetic photon detection for π^0 rejection.

1.2.2 E787 and E949 Detectors

The E787 and E949 detectors are well documented elsewhere[2, 6]; below is a brief review. To suppress the backgrounds, techniques were employed to incorporate redundant kinematic and particle identification measurements and efficient elimination of events with additional particles.

[1] The measured range is 34 cm < R < 40 cm and the measured energy is 115 MeV < E < 135 MeV.

The experiment employs an advanced design - low energy kaon beam and a sophisticated detection apparatus which is located inside a 1 T, 3 m diameter solenoidal magnet. E787 and E949 work at the 30 GeV Alternating Gradient Synchrotron of Brookhaven National Laboratory. The 730 MeV/c kaons are transported through the Low Energy Separated Beam (LESB3) with a K:π ratio about 4:1 [6].

Fig. 1.4 shows the side view and end view of the E787 detector. In order to identify the RSSCs location clearly, only half of the detector is depicted. The E949 detector is an upgrade of the E787 shown in Fig. 1.5. The function of the main sub-detectors are listed below.

- Čerenkov counter : Used to identify kaons and pions in the beam. The Čerenkov light is directed into 14 "K^+ phototubes" or 14 "π^+ phototubes", respectively.

- Two Beam wire chambers(BWPCs) : Used to identify multiple beam particles close to each other in space and time. For clean event selection, only one beam K^+ can be allowed to enter the detector. Principally, they are used to reject pions missed by the Čerenkov counter.

- Degrader : Slows beam particles so that kaons stop in the target. Also, the degrader absorbs the residual protons in the beam.

- B4 counter: Used for the beam K^+/π^+ identification by measuring the energy loss and time of entering the target.

- Stopping target : Kaons slow down and come to rest roughly in the center of the target, where they decay to π^+. A K^+ will travel along the fibers, depositing at least 5 MeV in each, and the outgoing π^+ will travel perpendicular to the fibers, depositing $\simeq$ 2 MeV in each. Thus, both the energy and space information is helpful to distinguish "K^+ fibers" from "π^+ fibers". Six I-counters surround

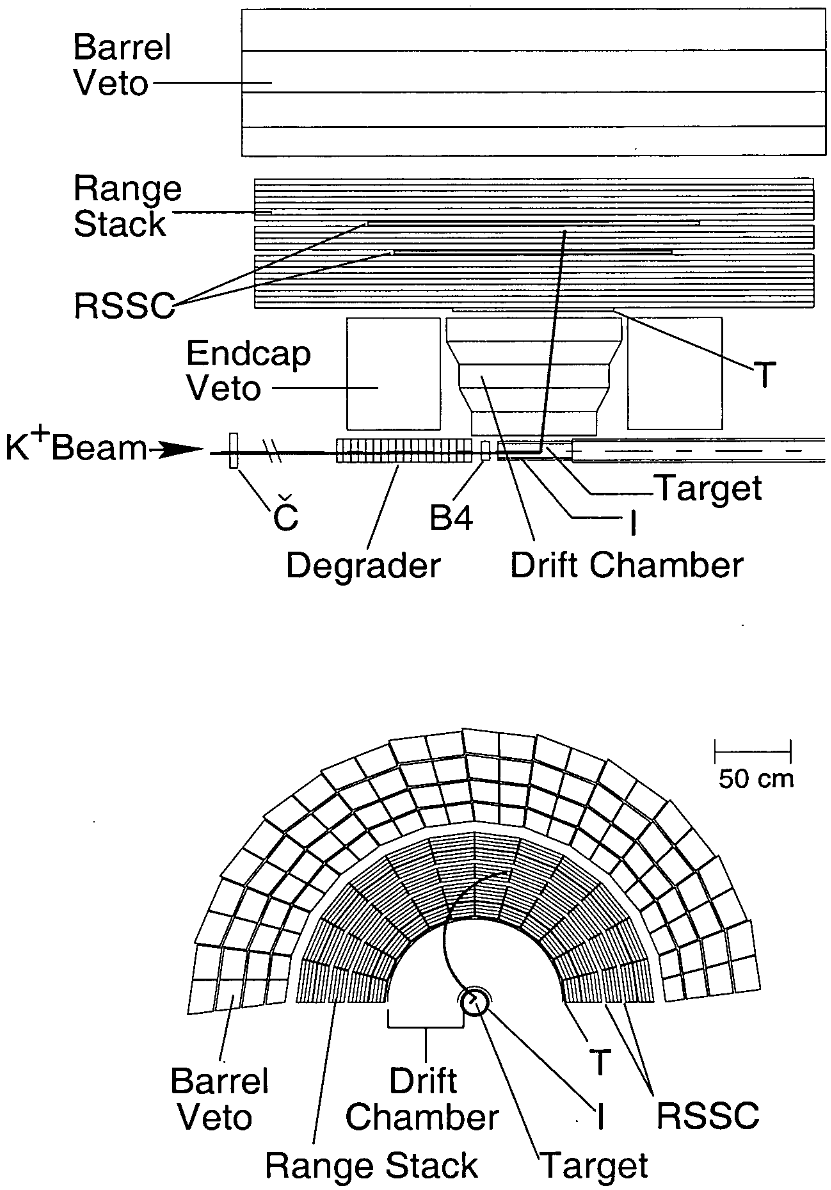

Figure 1.4: *Half side view and half end view of the E787 detector. RSSCs are located after the Range Stack layer 10 and 14[2].*

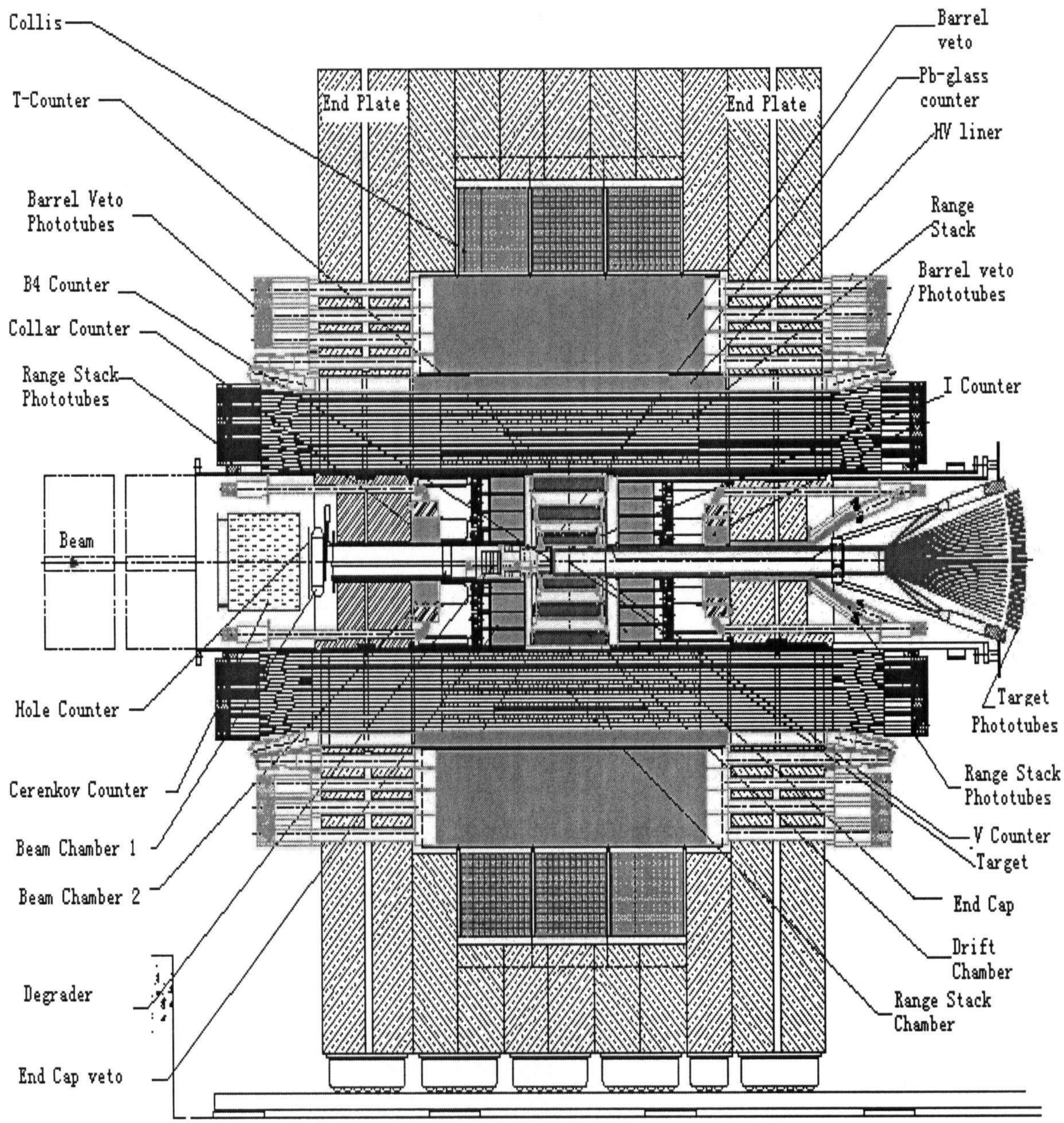

Figure 1.5: *Full side view of the E949 detector.*

the target hexagonally, are used to define the fiducial region of the target and measure the pion time used in the trigger delayed coincidence requirement.

- Drift chamber : The Ultra thin Chamber(UTC). Charged particles pass through the UTC creating the ionization electrons which drift to the anode wires with a constant velocity. From the drift time one can determine the drift distance from the charged particle trajectory to the closest hit anode wire. A number of hit anode wires (up to 12) depict the particle trajectory. Since little energy loss occurs in the UTC, the track is nearly circular and by fitting it, the pion transverse momentum P_{xy} is computed from $0.2999B_0$R MeV, where B_0 is magnetic field in kilo-Gauss and R is the radius in centimeters. The longitudinal momentum measurement is determined by measuring the dip angle from the cathode strip hits in six foil layers. Momentum is therefore calculated from $P_{xy}/\sin\theta_{dip}$.

- Range stack: The RS is used to slow down the π^+ and follow its decay at rest to a μ^+. The decay sequence $\pi^+ \to \mu^+ \to e^+$ is the most important feature used to reject muons. The range stack consists of 24 azimuthal "sectors" of stacks of plastic scintillator. Each stack has 21 radial layers. Two range stack straw chamber (RSSCs) layers are embedded in each sector to augment the range measurement by providing tracking information.

- Photon veto: A barrel veto and two endcaps surround the RS. They provide photon detection and energy measurements. This is an effective tool to suppress the $K^+ \to \pi^+\pi^0$ background since the π^0 will decay into two photons.

Range Stack Straw Chamber

2.1 Overview

2.1.1 RSSC geometry

The RSSCs were built at Princeton University. They are located after layer 10 (the inner RSSCs) and 14 (the outer RSSCs) of the RS, where most of the pions stop. The inner layer RSSC detector consists of 2 sublayers of 24 straw tubes per sector (see the end view in Fig. 2.1) and the outer one consists of 2 sublayers of 28 straw tubes per sector. Each straw tube is 3.4 mm in radius and has a 38-μm thick Kapton skin coated on the inside with Cu/Ni cathode together with a 50-μm diameter gold-coated tungsten anode wire. The mass per cm^2 is $0.054 g/cm^2$. The two sublayers of straw tubes are offset by half cell from each other so that high efficiency can be guaranteed. There are a total of 2×24 chambers, with 2496 straws installed in the E787/E949 experiments.

Figure 2.2 shows a top view of the RSSC. Two straws in the same sublayer are connected in pairs on the upstream end using a dedicated "jumper card". Connected straws are separated by either 12 or 14 straws, for the inner or outer chambers respectively, reducing the electronics channel count from 2496 straws to 1248 pairs. The chambers are read out from only the downstream end because of the severe space constraints and the desire to have the smallest possible cable length between the chambers and the external readout.

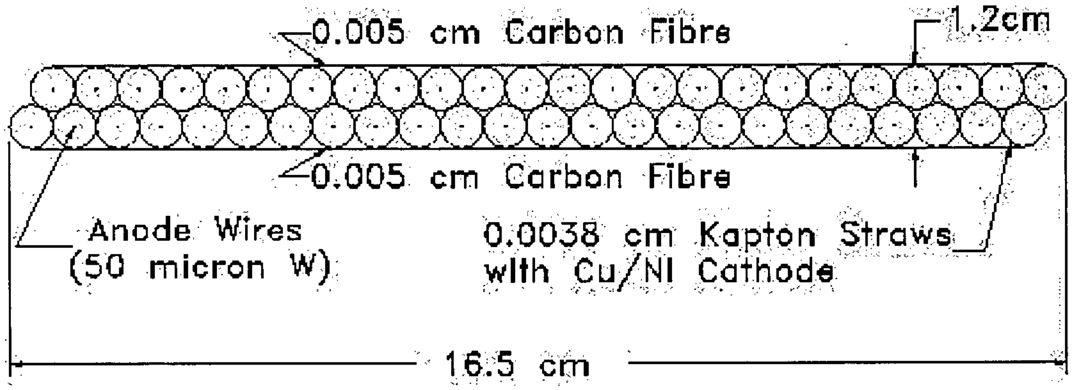

Figure 2.1: *End view of an inner RSSC[6]. Two sublayers of tubes are offset by half cell from each other.*

The advantages of this design are:

- The cells are isolated from each other by the 38-μm thick Kapton skins. Therefore, cross talk between cells along the anode wire is minimized.
- The structure of the straw chamber allows high spatial(xy) accuracy (as small as half the straw tube radius) and unambiguous localization in space.
- The resolution of tracks is independent of a particle's incident angle in the xy plane, so one does not have to incorporate angular correction factors.

2.1.2 RSSC readout electronics

The description of the readout electronics in this section is obtained from reference[6]. The E787 RSSC readout electronics include two parts. One is the front end electronics which is sketched on the top of Figure 2.3[1]. The other one is the external readout electronics which is sketched at the bottom of Figure 2.3.

[1] This diagram is sketched for one pair of straw tubes

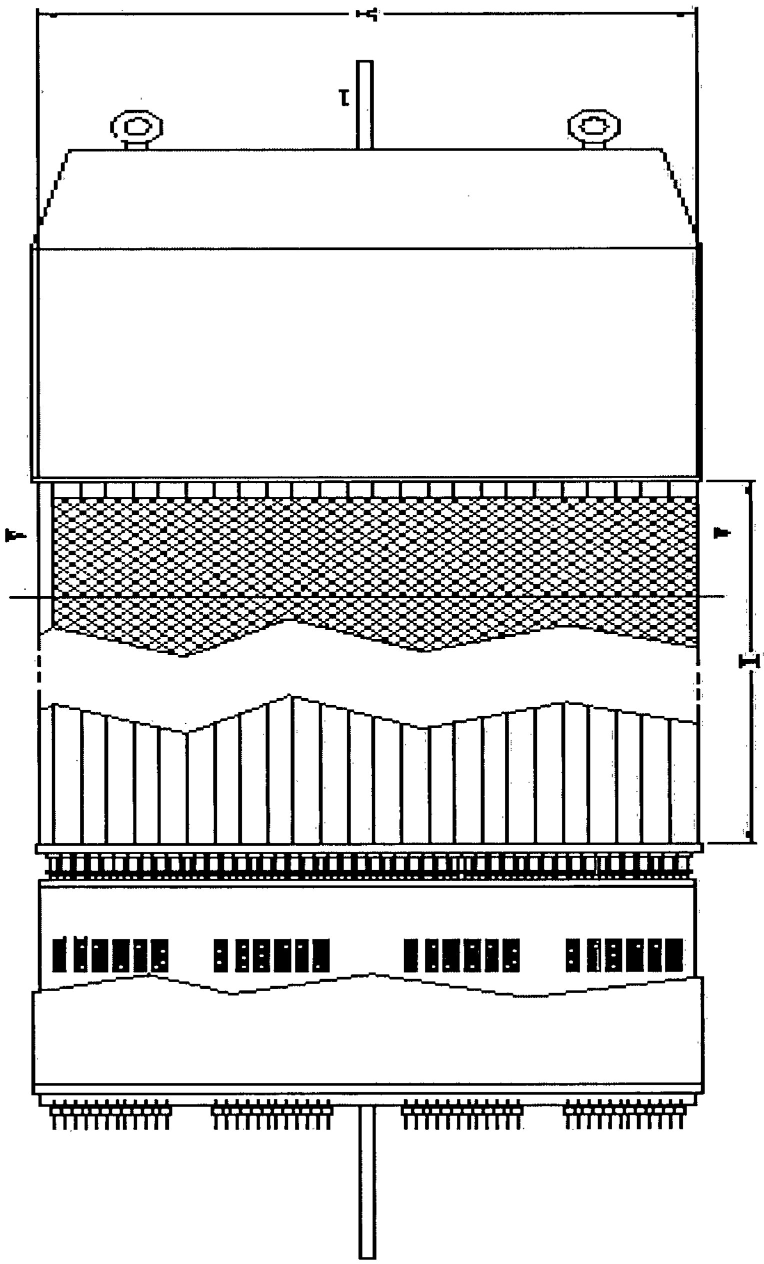

Figure 2.2: *Top view of an inner RSSC. The top part is the upstream end in which a "jumper card" is installed. The bottom part is the downstream end to which the external readout electronics are connected[6].*

Since the front end readout arrangement makes access to the chambers very difficult, no active electronics components are mounted on the chambers. There are no pre-amplifiers on the chambers. The front end consists of a single custom 2-layer readout-card, with a daughter board containing a set of sockets that line up with pins connected to the chamber wires that plug into the end of the chamber. This card takes up minimal space, and is part of the mechanical structure of the chamber itself. The straw walls are held at signal ground through a conductive-epoxy connection from the straws to an aluminum gas tight end-piece box, which is mechanically connected to the readout-card with small brass bolts. The high voltage is distributed onto a bus on the front-end card, and to each straw pair through a custom 10 MΩ surface-mount resistor. The signals pass through a custom surface-mount HV blocking capacitor, a resistor to match the straw impedance to the cables, and then through a connector built into the chamber to the cables themselves. The key elements in the front end are the custom surface mount resistors and capacitors used for HV distribution and blocking. While the resistors do not typical hold significant voltage, this custom thick-film elongated surface mount part is able to withstand HV sparks.

The analog signals are transmitted from the chambers through coaxial cables to the external electronics. There are 28 channels per external readout board. The first active electronics the signals see is a Lecroy MVL407 comparator. After forcing one end of the pair to always come late using a 25 nsec passive delay line, a time difference pulse is formed using a 10H131 ECL flip-flop. Note that the flip-flop clock is disabled while the primary time-difference pulse is being formed, so that the channel is disabled while the time stretcher is active, and the channel is self-reseting if no "late" pulse arrives. The primary time difference pulse is about 25 ± 7 nsec wide, with the z measurement encoded in that pulse width. This pulse is stretched by about a factor of 45 using a linear "Time Stretcher" circuit, making it about 1100 ± 300 nsec, which means signals from half of the chamber are always later than those from the other half. We call the former the late-tube half (i.e., the trailing edge time half) and the latter the early-tube half (i.e., the leading edge time half). With a modest 1 nsec resolution on the stretched pulse width, 20 psec resolution on the primary pulse width is obtained, which would be a 0.3 cm resolution z measurement. In practice, when running the chambers in the experiment, a 1 cm z resolution can be achieved. The crucial requirement in the external electronics is to be able to set the primary comparator threshold quite low, demanding a quiet circuit board and threshold voltage. To keep the board quiet, in addition to bypassing the power supply voltages, a ceramic 0.01 μF bypass capacitor is placed beside every power pin on the entire board. The level is set with a potentiometer on the board front-panel, and is shipped around at 100$\times$ the actual threshold level. It is divided down separately at each comparator input, and a 0.01 μF capacitor bypasses each channel's threshold to ground. Since any noise pickup on that long trace is also divided down, the threshold seen by the comparator is quiet. When the pulse arrives at the external electronics boards, the rough amplitude is 100 mV high and width is 30 nsec wide. The typical threshold is about 10 mV to suppress the noise. The other key feature is the linear time stretcher circuit. Its schematic is included in Fig 2.4. The complete readout system underwent a fairly severe set of tests done by the Princeton group: linearity, temperature variation, power supply voltage variations and magnetic field effects. The test results are listed in table 2.1.

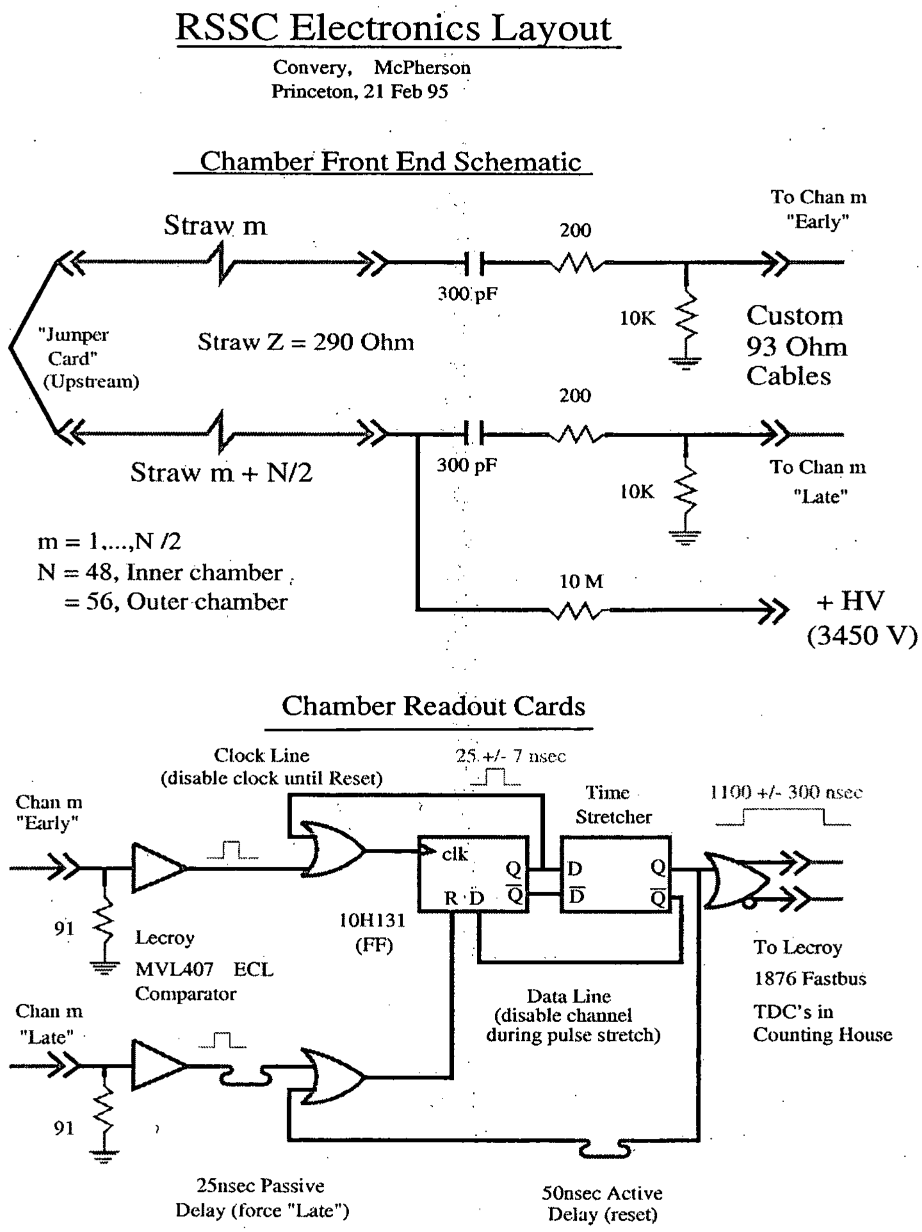

Figure 2.3: *RSSC electronics readout[6].*

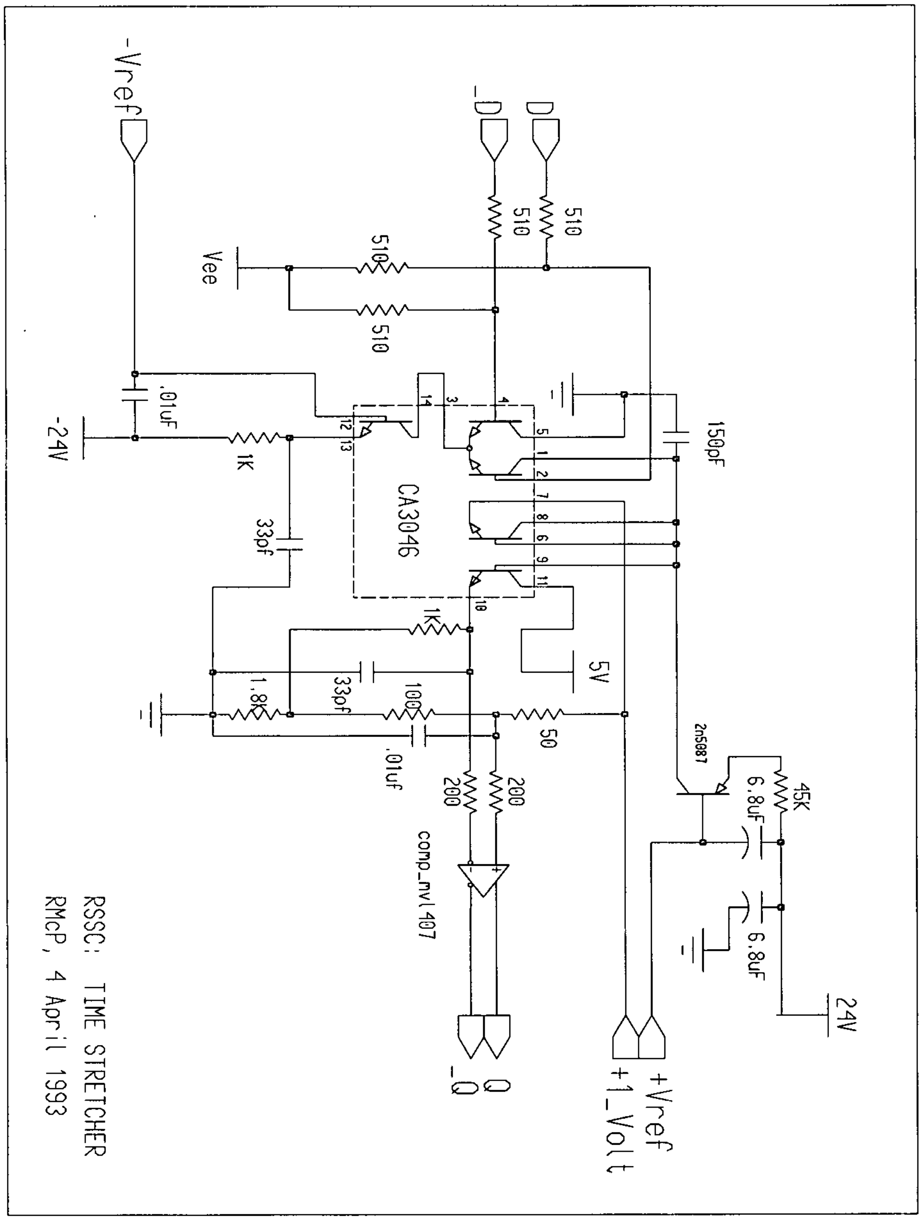

Figure 2.4: *The time stretcher schematic. The design is adapted from a Lecroy time-of-flight TDC. "Vref" is about 9 volts[6].*

Description	Results
Linearity	Typical Deviations from linear fit of $\pm$ 20 psec primary pulse width, over a range of 15-35 nsec widths
Temperature Variation	Better than $\pm$ 2 psec per degree Celsius primary pulse width, 5-35 degree Celsius
Power Supply Variation	-2 V supply: 1.5 psec per mV, primary pulse width -5.2 V supply: 0.2 psec per mV, primary pulse width rest: negligible
Magnetic Fields	No observable effects in fields up to 200 Gauss. (Stray field at electronics racks $<$ 20 Gauss)

Table 2.1: *Tests performed on the end-to-end time readout circuit[6].*

2.2 Limited streamer mode

2.2.1 Theory

The straw chambers are operated in limited streamer mode. The theoretical description in this section is reproduced from documents [10],[11],[12] and [13]. The model for streamer formation is based on Townsend gas discharge theory and space charge effects which distort the electric field near the anode wire and limit the electron avalanche[10]. The streamer nature of the discharge was established by Charpak et al.[11] and Fisher et al.[12]. It was observed that the centroid of charge generated by the process was definitely away from the center of the wire, suggesting a propagation from the wire towards the cathode. Atac[13] succeeded, by making use of image intensifiers, in obtaining a detailed picture of single streamers, which appeared as very thin ($\sim$ 200 μm) filamentary discharge channels, starting from the wire and propagating along a few millimeters towards the cathode.

Figure 2.5[14] gives a traditional picture of the streamer mode – the relationship between the high voltage and the gain of working in the proportional state and in the streamer state. At low voltage, the behavior is characterized by an exponential dependence on the high voltage. This is the proportional mode. At the high voltage end of the scale, there is a sudden transition to a mode of operation, where the charge collected on the anode is a linear function of the voltage. The output charge in this mode is less dependent of the initial ionization. This is the so-called limited streamer mode. Also indicated are two advantages for the limited streamer mode over the proportional mode. One is higher gain (up to 10^8) than that of proportional mode, the other is the collected charge is less sensitive to high voltage fluctuations.

The avalanche process is depicted in Fig. 2.6. The particle passes through the chamber and a cluster of ionization electrons is formed. The electron and ion mobilities differ by a factor of about 10^3. Thus, the electrons are collected on the anode wire in a few tens of nanoseconds, whereas the positive ions are essentially stationary during this collection time, creating space charge. The avalanche process follows the usual exponential behavior in the proportional region in Fig.2.5. The rate of growth of the avalanche slows down as the voltage exceeds a certain value indicating that space charge saturation is felt by the multiplying electrons, and cancels the applied electric field[15]. As a result, radiative recombination may occur. For instance, in a gas mixture Argon and isobutane, the process of recombination goes by the following reactions [13]:

$$A^+ + e^- \rightarrow A^* + \gamma \tag{2.1}$$

The energy of the emitted photons could be high enough to reach outside of the space charge cloud and produce electrons there from ionizing isobutane molecules[2] by the process:

$$\gamma + C_4H_{10} \rightarrow C_4H_{10}^+ + e^- \tag{2.2}$$

[2] Isobutane here serves as a quenching gas.

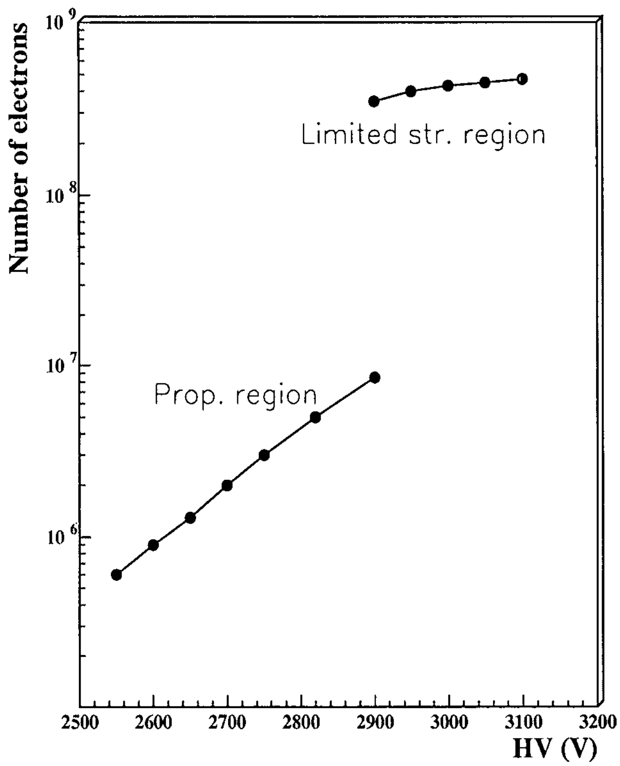

Figure 2.5: *Collected charge as a function of high voltage (a 100μm diameter wire in a tube* 12 × 12, *filled with* $Ar(49.3\%)+C_2H_6(49.3\%)+CH_3CH_2OH(1.4\%)$*). The exponential relationship is for proportional state and the linear relationship is for limited streamer state[14].*

These emitted electrons drift to the anode wire giving rise to the observed current signal.

The streamers quench themselves in a well controlled way providing uniform electronic pulses for a given energy loss from a traversing particle. Once the streamer process is triggered by the recombination photons, it will continue until the last such photon creates an electron at the streamer front. This streamer formation process is depicted in Fig.2.7

In short, in an iterative sequence, the amplification process develops towards the cathode and extinguishes itself with the proper gas mixture. Hence, the limited

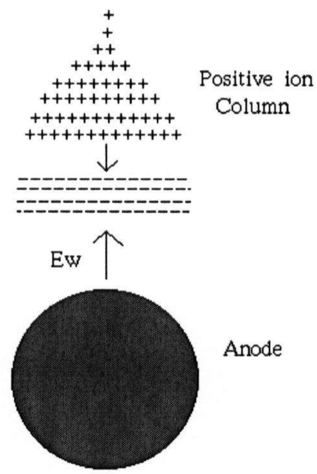

Figure 2.6: *Schematic diagram for the avalanche process.*

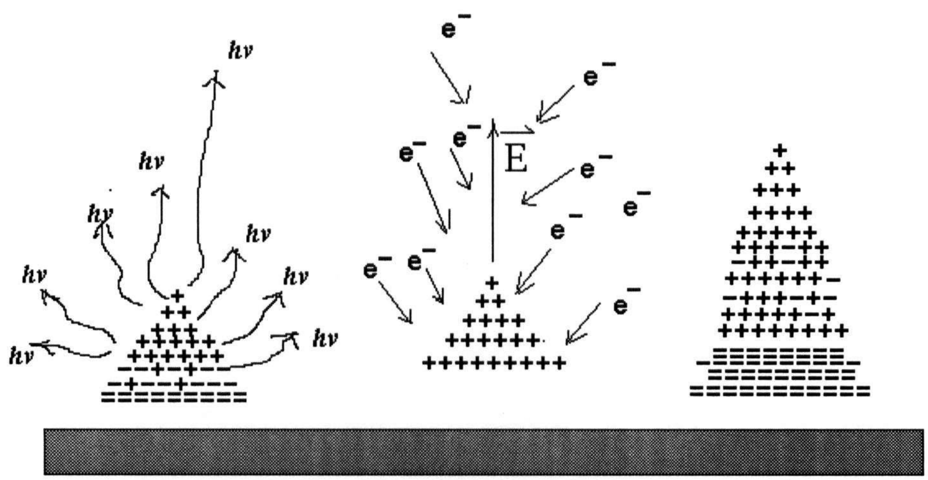

Figure 2.7: *Schematic description of the self quenching streamer phenomena.*

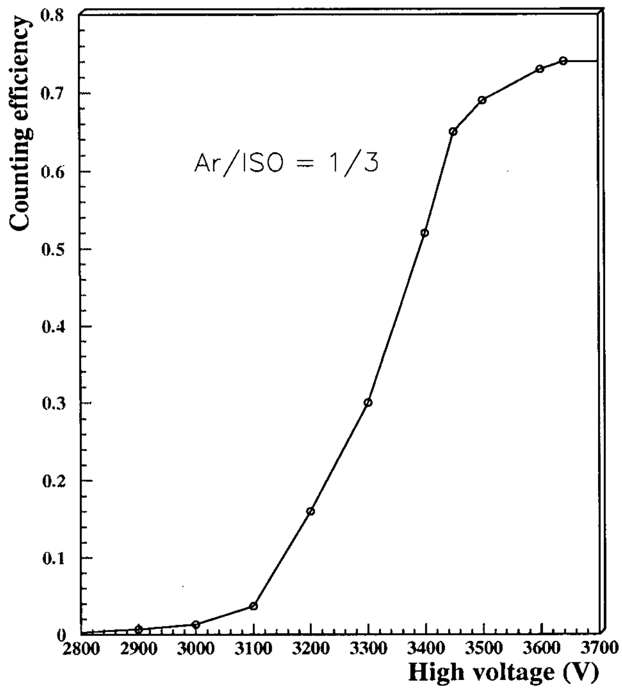

Figure 2.8: *Efficiency of counts vs high voltage.*

streamer mechanism is a consequence of a delicate balance of the electron avalanche in an electric field, which is dynamically adjusted by the avalanche process itself.

2.2.2 Chamber operation

The qualitative properties of the limited streamer operation depend on the wire diameter, the gas composition, the high voltage, and the cathode material. Below, only two main factors are discussed: the gas mixture and the high voltage.

A sufficiently quenching gas mixture is first needed in order to obtain stable, uncritical, and noiseless streamer operation. However, the quenching power is a function of the tube dimensions: the smaller the tube is, the bigger the quenching action will be. Taking into account that the streamer propagates from the wire toward the cathode, one can attribute the effect to the fact that the smaller the tube is, the shorter the streamer must be[3]. In practice, for small streamer tubes one is substantially left only with isobutane, with which undesired effects were rarely observed[16]. The isobutane as a quencher can absorb photons in the ultraviolet range (wavelength 100 - 200 nm), thereby reducing their range to a few wire radii ($\sim$ 100 μm). The transverse propagation of the discharge proceeds only in the vicinity of the anode wire because of the short traveling range of the photons. The photons have little chance to liberate electrons from the cathode via the photo-electric effect because they will be absorbed before they can reach the cathode. The E787/E949 RSSCs work with a gas mixture of 25% argon and 75% isobutane. The consequences of the high isobutane concentration are[17]:

1) very short wire pulse in duration, $\sim$ 50 ns into a 50 Ω load. The higher the quenching power is, the shorter the streamer formation is, leading to shorter pulse duration.

2) high working voltage. The high voltage provides the external electric field. At a certain high voltage, space charge is saturated. Higher quenching power means slower saturation. Thus, higher voltage is required to achieve similar behavior to those with lower quenching gas concentration.

Choosing the right operating voltage is the second factor affecting the straw chamber performance. Fig. 2.8 shows the typical counting rate curve as a function of the high voltage using a collimated ^{106}Ru source and setting the discrimnator threshold at 10 mV. The initial rise is due to the gradual transition from proportional to streamer operation. This effect continues increasing until the above transition is completed. The flat region corresponds to fully efficient streamer generation. The efficiency just above the knee (limited streamer mode) of the curve is around 70%. The efficiency, of course, depends on the threshold of the discriminator. The large amount of ionic

[3] Here the relevant gap is between the streamer tip and the cathode, which is fixed by the quenching action of the gas mixture[16].

charge developed in the streamer process introduces a large dead time, accounting for part of the reason for detection efficiency loss. The operating HV is chosen at 3450 V (just above the knee of the plateau). Beyond that, the tubes spark and the anode wires may be broken.

2.3 RSSC position measurements

The RSSCs are intended to give precise charged track measurement in the Range Stack (RS).

2.3.1 XY measurements

The coordinates in the RSSC xy plane depends on the sector number, i.e., each RSSC sector has its own xy coordinates. It is easy to transfer from the RSSC xy coordinates to the UTC xy coordinates[4] by a Lorentz transform since the angle between them for each sector is constant. The x axis is along the width of the RSSC and positive x points to the late-tube half[5]. Positive y points to the barrel veto detector[6].

The xy measurements of the charged track in the inner and outer RSSCs are used in the RS track reconstruction. If the xy positions in RSSCs can be determined, together with the entry point to the RS from the UTC extrapolation[7], the crossing

---

[4] It is the fixed experimental coordinates in E787/E949.

[5] See the description in section 2.1.2

[6] The barrel veto is the outermost detector as illustrated in Fig. 1.4

[7] In order to reconstruct a track in the RS, the entering sector of the RS producing the T.2 signal must be identified to notice the event coming. This is accomplished by identifying T counter (the innermost RS counter) and the RS layer 2 counter with hits close to the detector strobe time. Then, loop through drift chamber tracks and look for a match with a RS track. Thus, the entry point can be determined and its xy can be calculated

point of two RS sectors[8], a list of those RS counters that are part of the charged track[9] and the stopping counter[10], a hypothetical trajectory can be propagated through the RS using a simple model for energy loss that approximates the RS as a solid block of scintillator. The typical track reconstruction for a $K_{\mu 2}$ event in x-y plane from the UTC to the RS is depicted in Fig. 2.9.

The xy measurements in RSSCs are described in detail as follows:

- A charged particle may cause several tubes to be hit simultaneously. Therefore, one should find out the hits associated with a cluster first. A new cluster is defined by starting to search for a new chamber or if there is a gap between the adjacent hits to be greater than 3 $\times$ (straw radius). Hits are separated into clusters based only on their x positions.

- The individual x hits (e.g. for an inner RSSC) are calculated by formula "x = N_{wire} $\times$ radius" for positive x or "x = (N_{wire} - 23) $\times$ radius" for negative x[11] , where 'N_{wire}' is the wire number. Then, the cluster x position is calculated by averaging individual x.

- Then pick one cluster per RSSC layer according to which is closest to a series of arcs drawn from the UTC extrapolation to the T counter through the sector crossings. And that cluster average x is used as the true hit x position.

- The y values indicate the RSSC azimuthal radius which are 64.72 cm for the inner RSSC and 74.54 cm for the outer RSSC.

---

[8] Only positive tracks (bending towards lower sector numbers) are searched for. The xy coordinates of the first and second sector crossing needs to be calculated.

[9] This is done by performing a careful accounting of the energy deposited and the range of the charged track in the RS.

[10] The energy deposited in the last RS layer (called stopping counter) is used to estimate the range of the charged track in the RS.

[11] The reference point is the x position between the two middle straws in the first RSSC sublayer. For the inner RSSC, this is between the early half of channel 23 and the late half of channel 0.

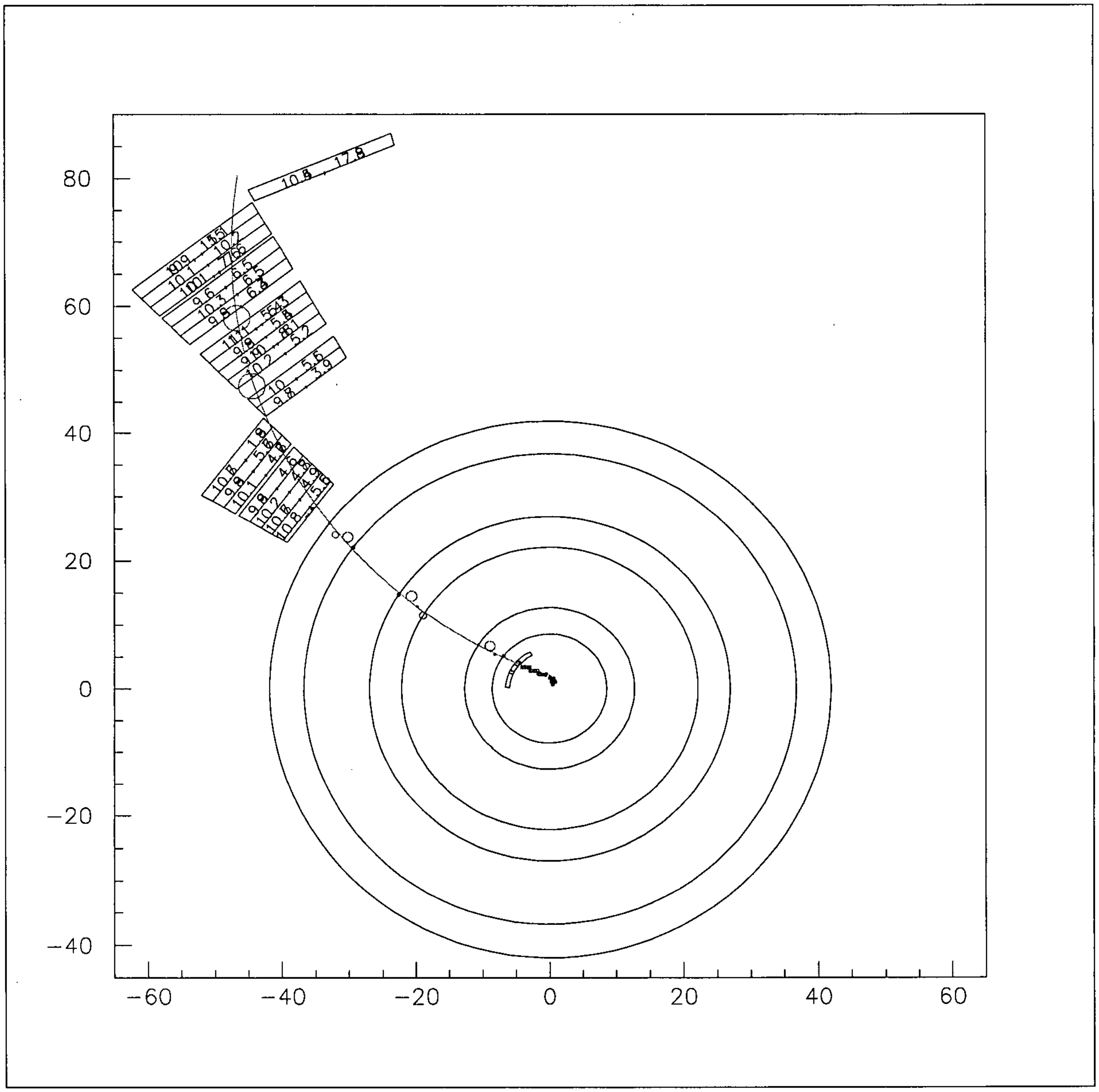

Figure 2.9: *A typical $K_{\mu 2}$ event reconstruction, showing the charged track trajectory from the target to the RS in the x-y view. The large circle depicts the 3 super-layers of the UTC. Isochrones are depicted as the small circles within these super-layers. The thin boxes are the RS counters. There are two large circles between the RS counters which depict the hits in the inner/outer RSSCs. Using the entry point, the crossing sector point, each RS hit counters and two RSSC hits, the range in the RS can be obtained and the charged track reconstructed in the RS.*

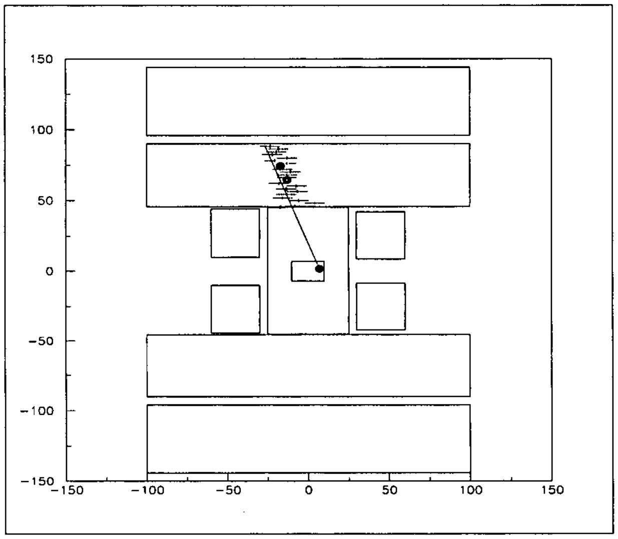

Figure 2.10: *The r-z view shows the z information of the same $K_{\mu 2}$ event. The center smaller rectangle is the target. The center larger rectangle is the UTC. The four small rectangles in the middle part are the end-caps. The inner big rectangles are the RS and the outer big rectangles are the barrel veto.The RSSC hits are labeled using two dark circles to show them clearly.*

2.3.2 Z measurement

The z axis is defined to be along the direction of the kaon beam. Positive z points to the downstream end. For the longitudinal (z) measurement, hits are only considered if they are prompt and have "reasonable" z measurements[12].

The RSSCs use end-to-end timing to get the z information as illustrated in Fig. 2.11. When a particle hits a tube, signals travel to the downstream and the upstream ends, respectively. Since both signals are read out from the downstream end, one of them always travels a longer distance than the other. The time difference from the trailing and leading edges is proportional to the hit position for a given propagation speed in each tube.

Suppose the whole tube length is l_0, the velocity is v_0, the signal travel distance

[12] The measured time is between 10 - 90 ns and the valid $|z| < 75$ cm. Both of these cuts are rather loose.

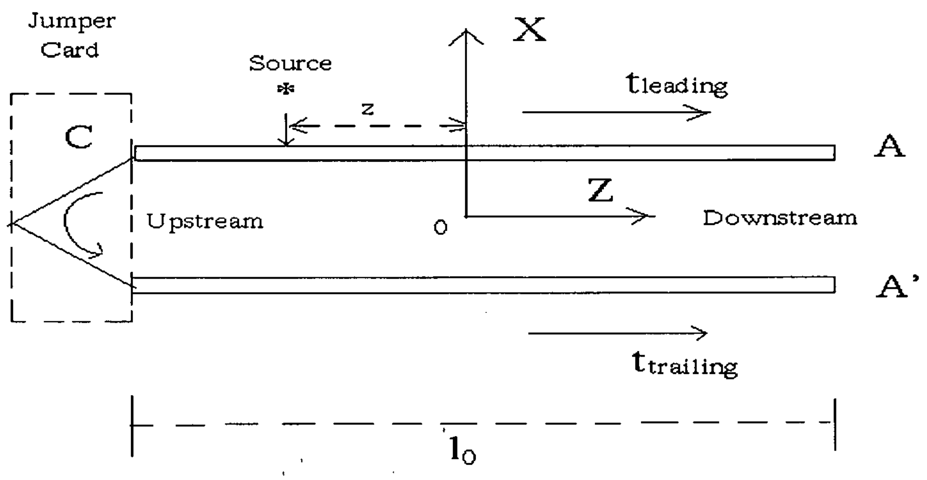

Figure 2.11: *RSSC schematic diagram of the end-to-end timing method.*

in the jumper card (the C part in Fig 2.11) is c_0, and the recording times in TDC are $t_{leading}$ and $t_{trailing}$, corresponding to the signals from end A and end A' respectively. The hit z position can be figured out using the following equations:

$$v_0 t_{trailing} = l_0 + (\frac{l_0}{2} + z) + c_0, \tag{2.3}$$

$$v_0 t_{leading} = (\frac{l_0}{2} - z). \tag{2.4}$$

Subtraction Equation 2.3 from equation 2.4 gives:

$$v_0(t_{trailing} - t_{leading}) = l_0 + 2z + c_0 \tag{2.5}$$

Thus,

$$z = \frac{v_0 \Delta t - (l_0 + c_0)}{2} \tag{2.6}$$

$$z = K\Delta t + B \tag{2.7}$$

where $\Delta t = t_{trailing}$ - $t_{leading}$; the slope K = $v_0/2$ is the effective velocity; the intercept B = -(l_0+c_0)/2 is the effective length.

In E787, the RSSC z is calculated by a weighted average of the individual z hits in a cluster, taking into account their uncertainties. The r-z reconstruction of the same $K_{\mu 2}$ event as in Fig. 2.9 is depicted in Fig. 2.10.

The RSSC z information is used to make a useful cut on the residual of (Z_{UTC}-Z_{RSSC})[13] to separate large angle scattering muons from pions.

[13] It is the difference between the z positions from the track of the UTC extrapolated to the RSSCs and the z positions of hits in the inner and outer RSSCs.

The solution to the poor RSSC z position measurements

3.1 The RSSC measurements in E787

3.1.1 History

In E787, The quality of the RSSCs' z measurement can be checked by using a $K_{\mu2}$[1] sample, requiring the muon momentum, range and energy at the right position within 3 σ[2]. Fig. 3.1 shows the residual (Z_{UTC} - Z_{RSSC}). If the chambers were working correctly, we would expect a Gaussian distribution, centered at zero. However, there are three problems:

- First, the mean difference is not zero in both cases, suggesting that the z calibrations of the RSSCs with respect to the UTC are incorrect. This can easily be remedied.

- From Monte Carlo simulation, the resolutions of the residual for $K_{\mu2}$ data are 1 cm. The much worse observed resolutions indicate there may be some unexpected contributions to the RSSC z measurement.

[1] For the $K_{\mu2}$ sample, events are required not to be a beam background, no photon detected and particles are well reconstructed and identified not to be pions with momentum > 211 MeV/c, Range > 33 cm and energy > 115 MeV.

[2] The requirement removes events suffering large angle scattering. Therefore, those suffering the multiple scattering events should show a normal distribution.

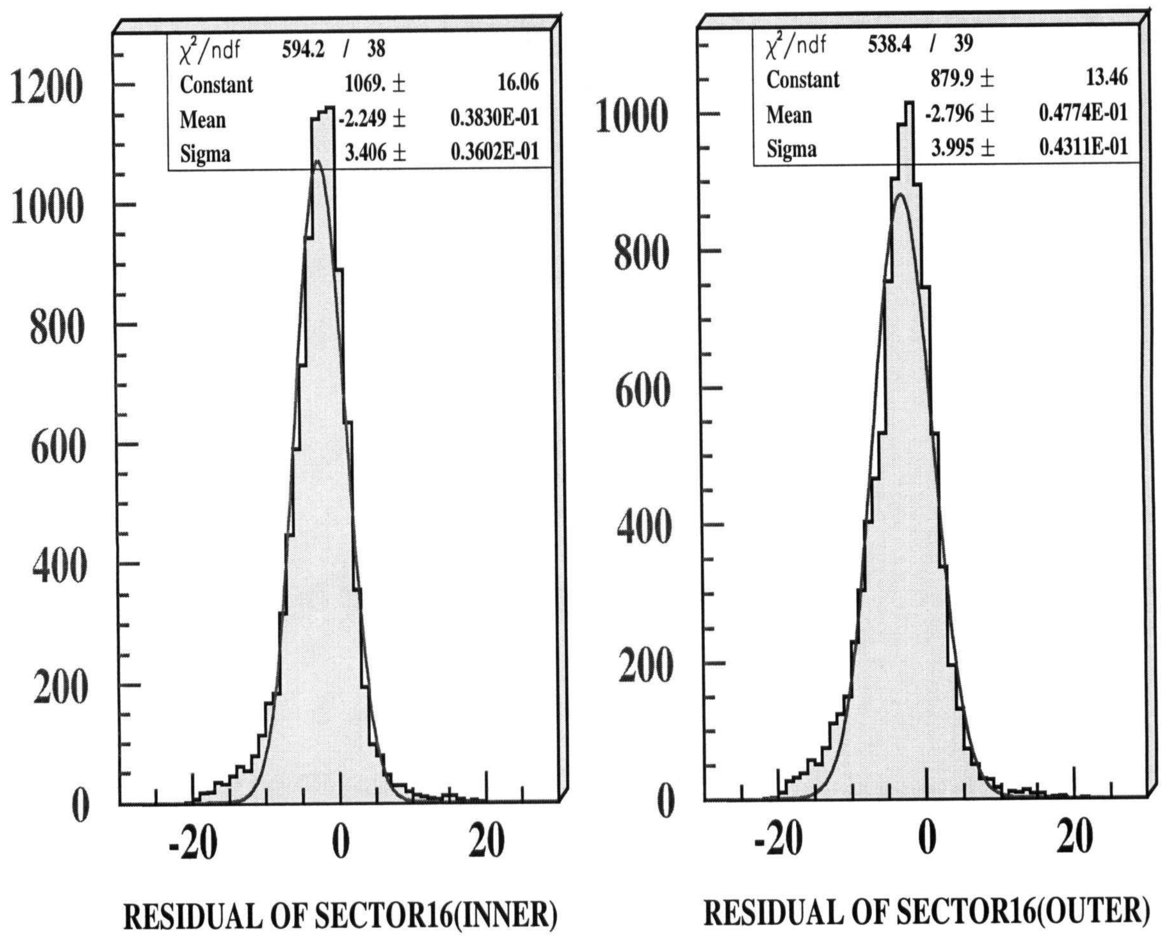

Figure 3.1: *Residual (Z_{UTC} - Z_{RSSC}) from the $K_{\mu 2}$ sample. The left one is for the inner RSSC and the right one is for the outer RSSC.*

- More troubling is that the distributions are not well fit by Gaussians. The tails in the distributions indicate that the RSSCs sometimes badly misreconstruct the z positions. The large tails on the left side of peaks mean an excess of events in which the z position of the RSSC cluster is significantly downstream of the z position of the extrapolated UTC track[18].

3.1.2 Study of pion samples

The residual (Z_{UTC} - Z_{RSSC}) resolutions of $K_{\pi 2}$[3] from the Monte Carlo simulation and from a 1998 data sample were studied to unfold what is behind the poor resolution.

The distributions of the residual are plotted in Fig. 3.2 and Fig. 3.3 . The resolutions of the residual are listed in Table 3.1.

The worse observed resolutions indicate that there are contributions, other than physics contributions[4], to the z measurements, which can be represented by the differences[5] between the MC and the data in the third column of Table 3.1.

In the third column, the downstream ends show worse resolutions than those on the upstream ends. The RSSC electronics contributions on the upstream and downstream ends should be identical, considering the fact that the upstream and the downstream share the same electronics channel. The worse results on the downstream ends indicate that the contributions include an unknown source, other than the RSSC electronics contribution. And the unknown contribution has a larger impact on the downstream ends. An explanation will be given in section 3.2.1.

Also, in the third column, better resolutions can be obtained in the outer RSSCs. However, in the MC, the outer RSSCs show worse resolutions due to greater multiple scattering. And the electronics contributions from the inner and outer RSSCs should be identical due to the similar electronics. The better performance in the outer RSSCs indicate the unknown contribution overrides the physics contributions and has a smaller impact on the outer RSSCs. An explanation will be given in section 3.2.1.

---

[3] For the $K_{\pi 2}$ sample, events are required not to be a beam background, have photon detected and be well reconstructed and identified not to be muons with momentum < 211 MeV/c, Range < 33 cm and energy < 115 MeV.

[4] Physics contributions to the z resolution include the π^+-nuclear interaction and multiple scattering effects in the range stack, which can be simulated by the Monte Carlo simulation.

[5]

$$\Delta\sigma_z = \sqrt{\sigma^2_{data} - \sigma^2_{umc}}. \tag{3.1}$$

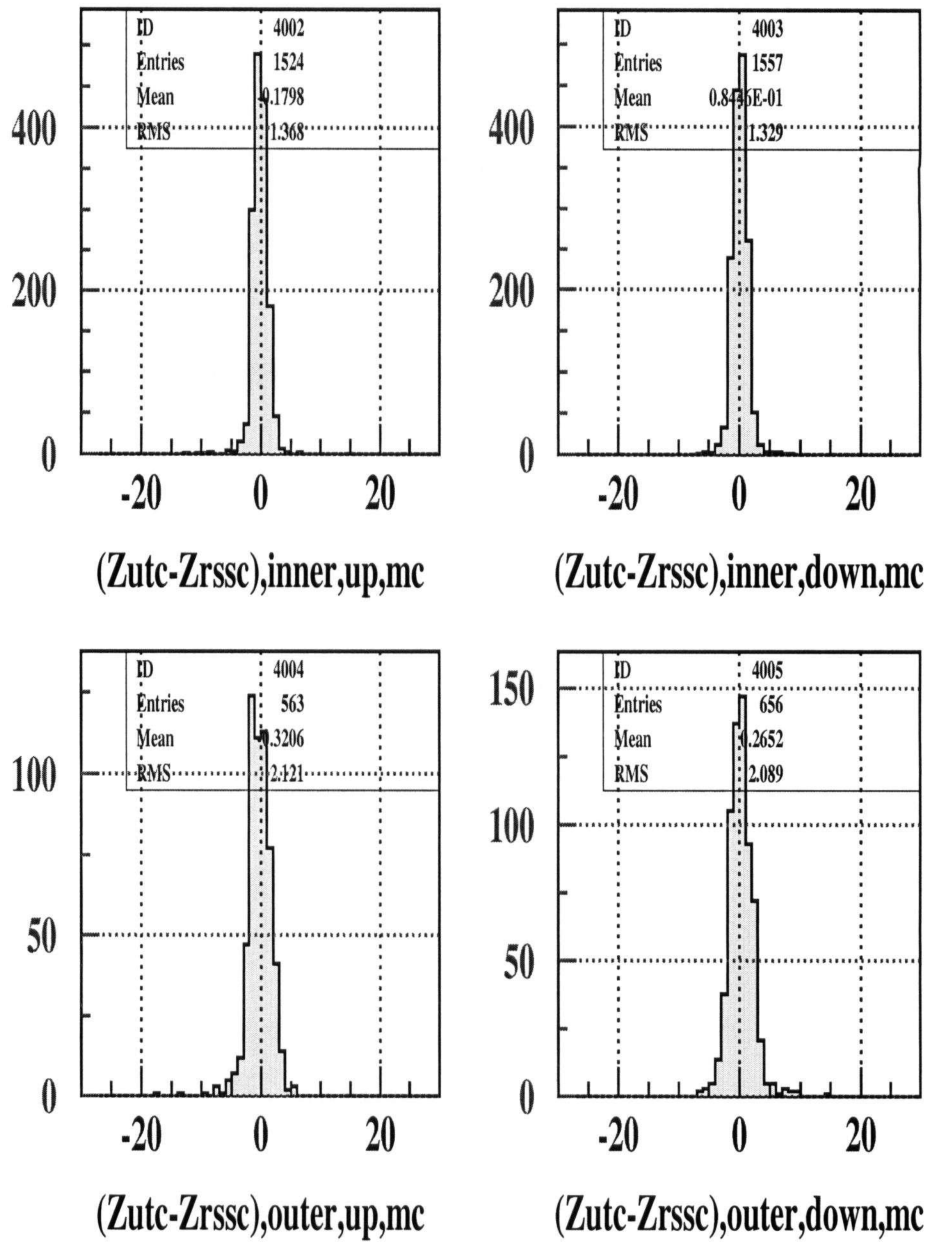

Figure 3.2: *Residual (Z_{UTC} - Z_{RSSC}) of the $K_{\pi 2}$ sample from the Monte Carlo simulation. 'Inner' indicates the inner RSSC; 'outer' indicates the outer RSSC; 'up' indicates the upstream end; 'down' indicates the downstream end; 'mc' indicates the Monte Carlo simulation.*

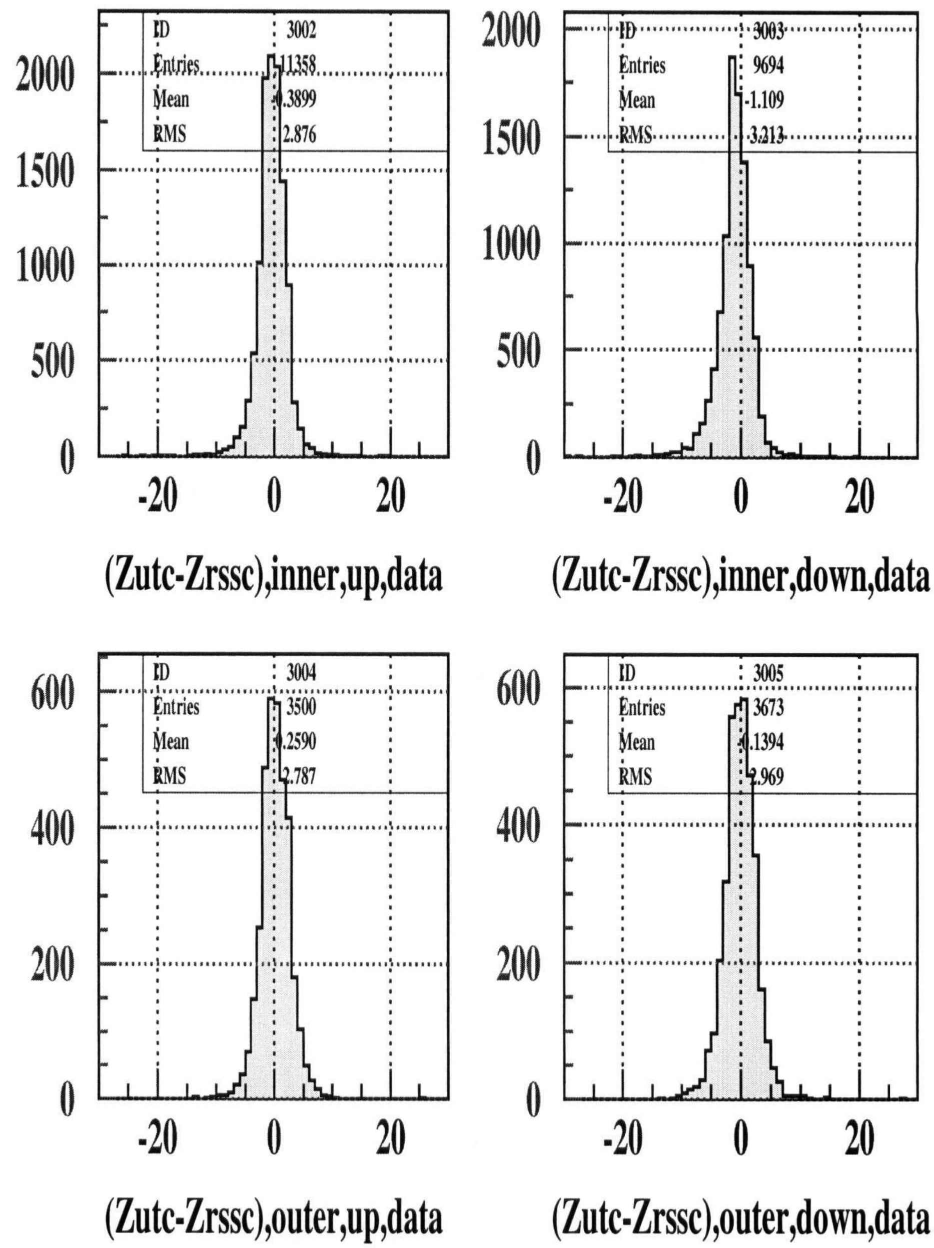

Figure 3.3: *Residual of Z_{UTC} - Z_{RSSC} from 1998 data for the $K_{\pi 2}$ sample.'Inner' indicates the inner RSSC; 'outer' indicates the outer RSSC; 'up' indicates the upstream end; 'down' indicates the downstream end; 'data' indicates the 1998 data.*

	σ_z(M.C.) (cm)	σ_z(Data) (cm)	$\Delta\sigma_z$ (cm)
Inner upstream	1.37	2.88	2.53
Inner downstream	1.33	3.21	2.92
Outer upstream	2.12	2.79	1.81
Outer downstream	2.09	2.97	2.11

Table 3.1: *Residual (Z_{UTC} - Z_{RSSC} resolution of the $K_{\pi 2}$ from the Monte Carlo simulation and from a 1998 data. Upstream is defined as $z < 0$, while downstream is defined as $z > 0$. $\Delta\sigma_z$ is the difference of the z resolution between the first two columns.*

	σ_z(Muon) (cm)	σ_z(Pion) (cm)
Inner upstream	4.44	2.88
Inner downstream	4.62	3.21
Outer upstream	6.29	2.79
Outer downstream	6.37	2.97

Table 3.2: *Residual (Z_{UTC} - Z_{RSSC} resolution comparison between the large angle scattering muon sample and the $K_{\pi 2}$ sample.*

3.1.3 Contributions to the resolution

In order to figure out what contributes to the resolution, the muon tail sample and $K_{\pi 2}$ sample were studied. The muon tail sample includes muons suffering large angle scattering in the RS. The measured range and energy are far below the expected peak positions, leading to muons migrating into the pion signal region. Fig. 3.4 clearly shows this phenomenon. In this figure, the different kaon decay modes are described by different clusters or bands. The large angle scattering muons from $K_{\mu 2}$ and $K_{\mu\nu\gamma}$ migrate into the pion range indicated by the rectangle.

Results from large angle scattering muon sample and $K_{\pi 2}$ sample are listed in Table 3.2.

The unknown contribution to the z measurement is hypothesized to be due to the different energy loss dE/dX for the low momentum muons and pions. For a given momentum, since the mass of the pion is greater than that of the muon, $1/\beta^2$ for

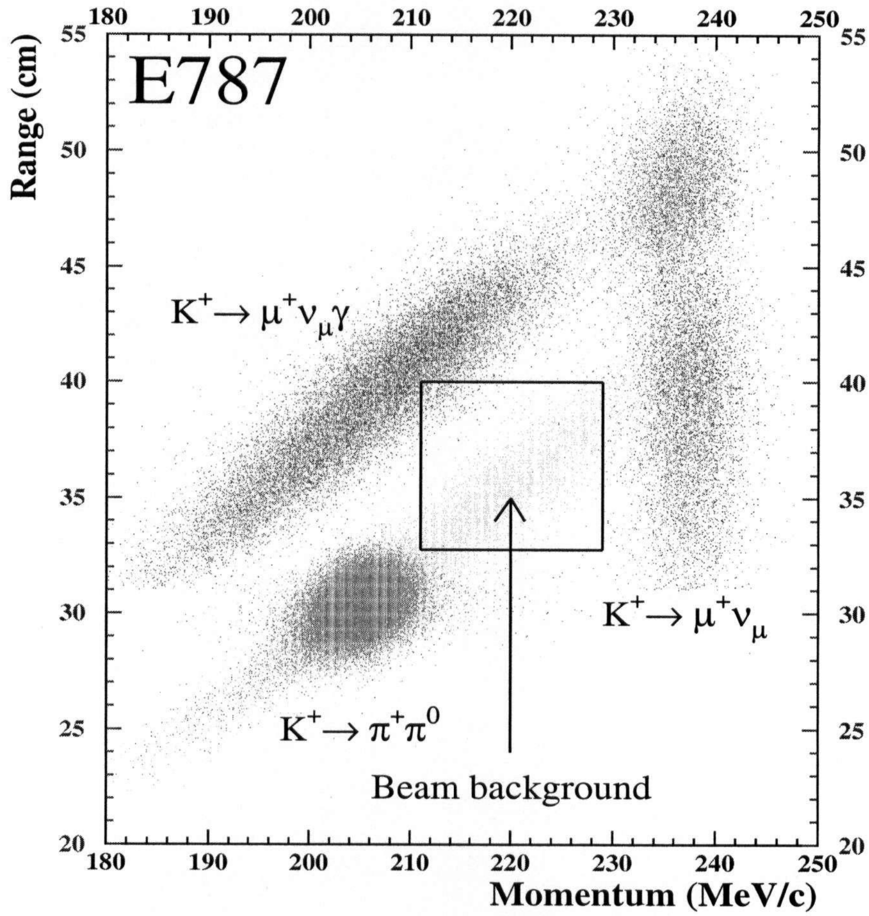

Figure 3.4: *The measured range of the different kaon decay modes. The large angle scattering muons from $K_{\mu 2}$ tail and $K_{\mu\nu\gamma}$ band migrate into the rectangle pion range.*

the pion is greater than that for the muon, where β is v/c. From the Bethe-Bloch equation (Equ. 3.2),

$$-\frac{dE}{dX} = Kq^2\frac{Z}{A}\frac{1}{\beta^2}\left[\frac{1}{2}ln(\frac{2m_e\beta^2\gamma^2E_{max}}{{I_0}^2}) - \beta^2\right], \tag{3.2}$$

where Z is the atomic number, A is the atomic mass, q is the charge number and

$$\gamma = \frac{1}{\sqrt{1-\beta^2}}. \tag{3.3}$$

Energy loss is approximately proportional to $1/\beta^2$, resulting in relatively higher energy losses for pions (typically 50% higher). Thus, it was suspected that the better z measurement observed for pions was due to larger energy loss which suggests that the pulse amplitude may affect the z measurement in the RSSCs.

3.1.4 Further study about contributions to the resolution

It is hypothesized that the unknown contribution to the RSSC z resolution depends on pulse amplitude. The larger the amplitudes are, the better the resolutions are.

Bench tests were done using an ^{55}Fe source[6] and a ^{106}Ru source[7] to confirm this conclusion. Sources were put on the tube 1, tube 2 and tube 3 of the RSSC on the downstream, middle and upstream positions, respectively. The z measurement resolutions, listed in Table 3.3, show the results from the ^{55}Fe source was better than that from the ^{106}Ru source due to the fact that the signal amplitudes of the former are much larger than the latter's.

Thus, if we can increase the signal amplitude, better z measurement can be

[6] For the ^{55}Fe source, only one tube is hit per event. ^{55}Fe decays via electron capture to ^{55}Mn, which de-excites and produces a 6 keV K x-ray. If the x-ray is captured in the chamber gas, a localized ionization avalanche is created, resulting in a pulse resembling one from a charged track in the straw.

[7] As for the ^{106}Ru source, the situation is similar to the E787/E949 circumstance since the ^{106}Ru emits electrons which pass through the chamber and create limited streamers in the chamber gas.

position	resolution from an ^{55}Fe source			resolution from a ^{106}Ru source		
z (cm)	W_1	W_2	W_3 (cm)	W_1	W_2	W_3 (cm)
36	0.94	1.21	0.94	3.81	5.90	4.61
2.0	0.64	0.95	0.75	2.59	2.70	3.00
-34	0.70	1.17	0.81	2.64	2.15	2.35

Table 3.3: *Z resolution comparison from an ^{55}Fe source and a ^{106}Ru source for an inner RSSC. The former resolution was better than the latter's due to the larger amplitude. W_1 indicates tube 1. W_2 indicates tube 2. W_3 indicates tube 3.*

achieved. One possible solution is to increase the high voltage. The E787 RSSCs system would work well if we could increase the voltage gain. As explained in the chapter 2, the higher gain means more ionizated electrons collected on the anode wire per event, giving a larger pulse amplitude. For example, in bench tests, the pulse amplitude of an ^{55}Fe source is about 28 mV at 3000 V and is about 60 mV at 3450 V. However, this approach is infeasible due to the RSSC breakdown at higher voltage.

3.2 Explanations

3.2.1 Time walk

Based on the image from the true pulses shown in Fig. 3.5, an explanation to the poor z resolution may be given - the resolution depends on the signal amplitudes due to time walk. The pulse images, in Fig. 3.5, show the leading edge timings from two adjacent channels shifting because of the different amplitudes.

Consider, for example, two signals of different pulse height but exactly coincident in time as shown in Fig. 3.6. Suppose these signals are introduced into a discriminator with a fixed threshold. Because of the difference in amplitude, signal A will trigger at time t_a and signal B will trigger at t_b, although both are exactly coincident. The dependence on amplitude causes the logic signal to "walk". This phenomenon

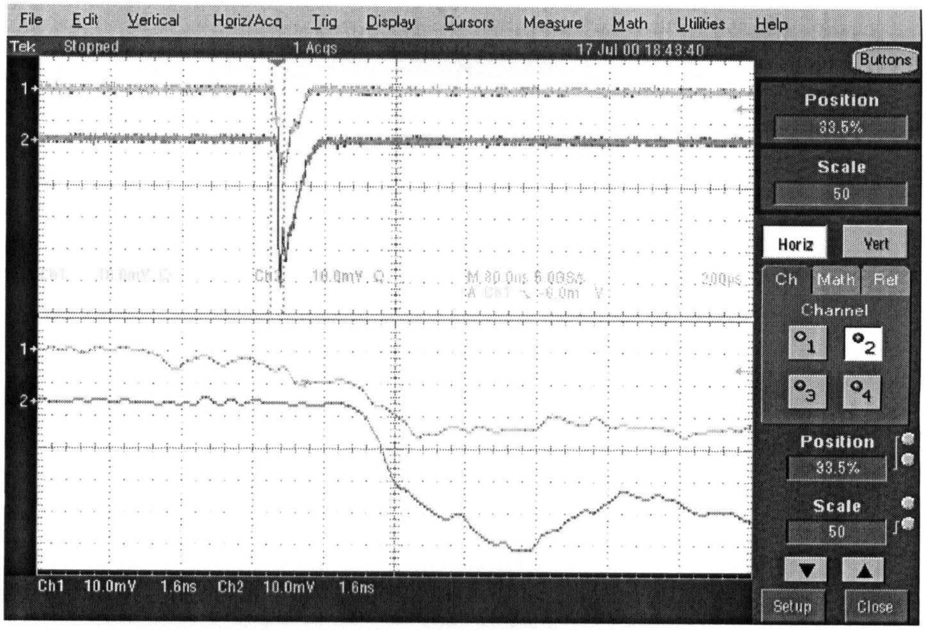

Figure 3.5: *Typical RSSC pulses from two adjacent straws. Different amplitudes result in time shift due to the fixed discriminator threshold. The bottom two curves are the part between two vertical dashed lines in the falling edges of the top two curves, which are enlarged to show the time shift clearly.*

contributes to the poor RSSC z resolution.

Then, we can answer the questions left in section 3.1.2. For the downstream end, the worse resolution is due to the greater attenuation and dispersion of the signals. When a hit occurs on the downstream end, the time difference from the trailing and leading timing is larger than that when a hit occurs on the upstream end. Thus, the amplitude difference is greater on the downstream end than that on the upstream end. Hence, larger time walk occurs when hits are on the downstream end leading to the worse z measurements. Likewise, the better resolutions in the outer RSSCs is because the smaller traversing velocities (the larger energy losses) in the outer RSSCs give larger pulse amplitudes leading to smaller time walk.

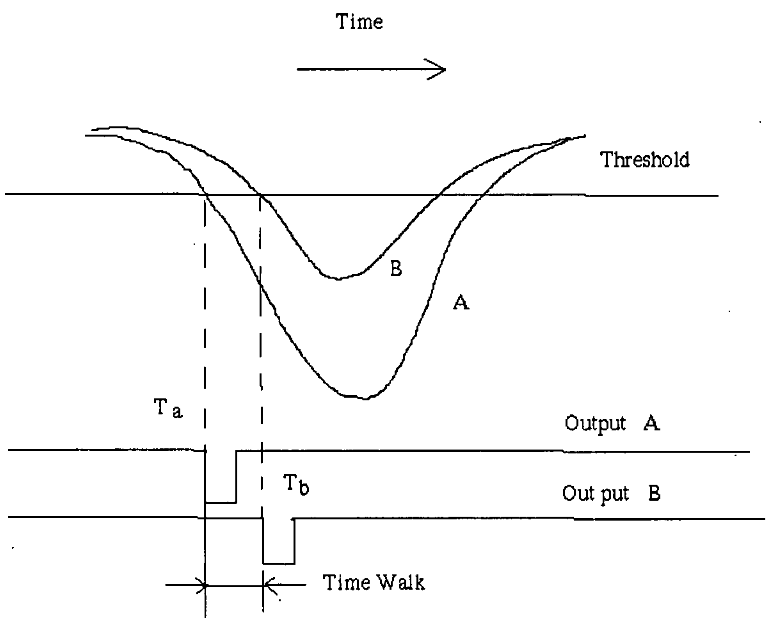

Figure 3.6: *Schematic diagram of the time walk effect.*

3.2.2 Cross talk

When a particle hits a tube, a small amplitude cross talk can be induced in its neighbors. Each straw tube is isolated from the others by a metal isolating film, minimizing the possible cross talk along the tube. However, the connection of the straw pairs on the upstream end (the connection in the jumper card) and the connection between the chamber and the external cables have little shielding protection. Cross talk may occur at any of the three positions (A, A', C) indicated in Figure 2.11.

For the E787 RSSC system, cross talk was suppressed by a high discriminator threshold and can be negligible. As introduced in section 2.1.2, the threshold of the comparator on the external electronics board was set at 10 mV for suppressing the noise and cross talk in E787. Let's verify that 10 mV is a suitable value to suppress cross talk in the E787 RSSC system.

A collimated ^{106}Ru source was put on the tube 1[8] of an inner RSSC to investigate

[8] Tube 1 indicates the first tube on the top sublayer of the RSSC from right to the left in Fig. 2.1, while tube 2 indicates the first tube on the bottom sublayer of the RSSC from right to the left in

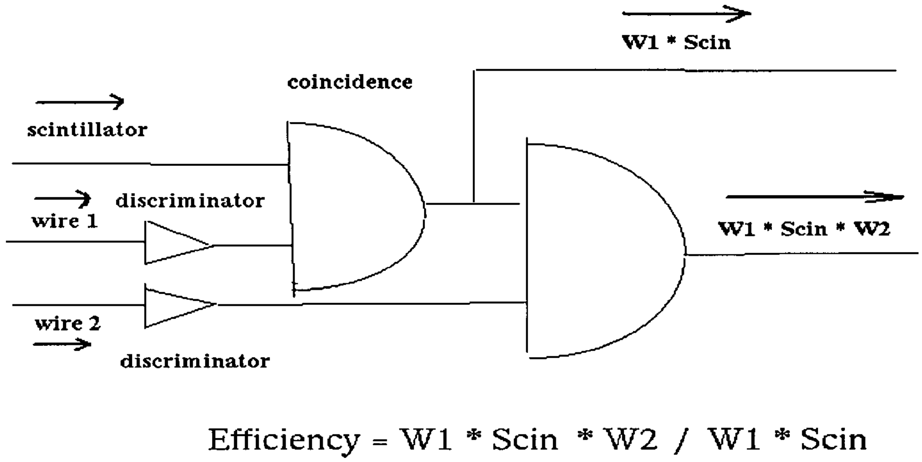

Figure 3.7: *The definition of the cross talk count rate. 'W_1' indicates the hits on the tube 1, 'W_2' indicates the hits on the tube 2 and 'Scin' indicates the hits on the scintillator. Tube 1 and the scintillator were used as a trigger.*

the behavior of cross talk in tube 2 varying with the tube 2 discriminator threshold. The definition of the cross talk count rate is shown in Fig. 3.7. The curve in Fig. 3.8 dropped down because cross talk was removed when raising the tube 2 discriminator threshold. The flat curve above 10 mV indicates that almost all cross talk was removed. And it can't drop to zero due to the fact that a particle usually hits two tubes which are located at different sublayers of the RSSC simultaneously (i.e. tube 1 and tube 2 in this case.). Thus, 10 mV was a suitable value to suppress cross talk in the E787 RSSCs.

Fig. 2.1.

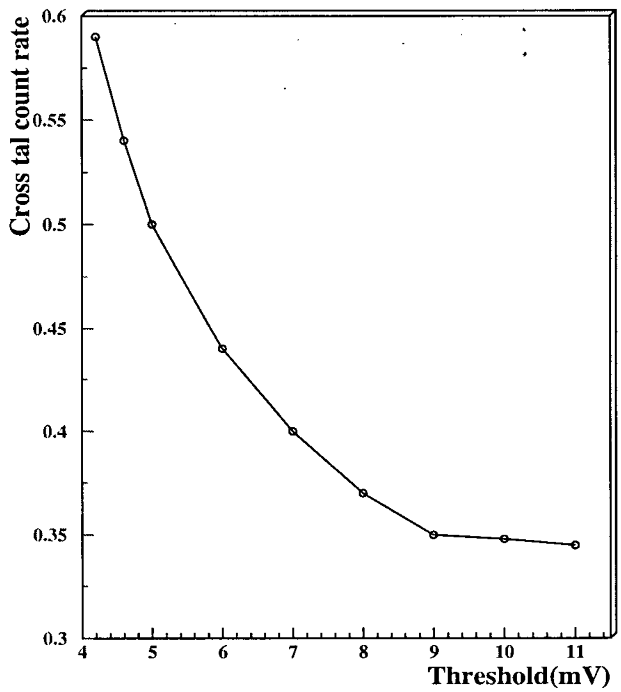

Figure 3.8: *Cross talk count rate vs tube 2 high threshold. The source was on tube 1.*

3.3 Add-on board

From section 3.2.1, one can conclude that the larger the signal amplitudes are, the smaller time walk is. Thus, a possible solution is to add amplifiers to the E787 RSSCs. However, cross talk can also be amplified simultaneously.

In order to get around this shortcoming, the TRIUMF group designed an add-on board with two discriminators for each channel to go between the chamber and the existing external electronics. A high threshold eliminates cross talk and a low threshold is used to minimize time walk. Fig. 3.9 shows the circuit diagram for a typical channel.

3.3.1 Working principal

This add-on board has 56 channels, including two amplifiers, a high-threshold discriminator, a low-threshold discriminator, a delay line and a coincidence.

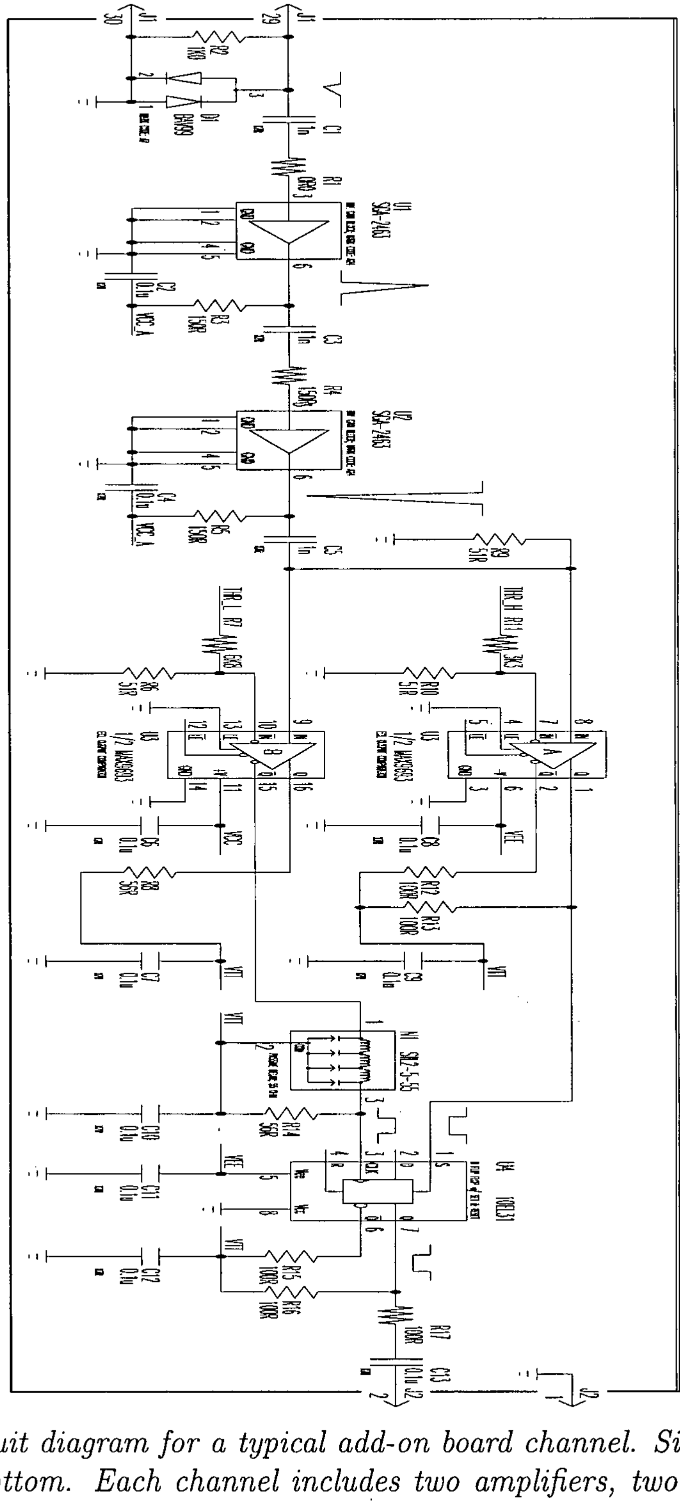

Figure 3.9: *Circuit diagram for a typical add-on board channel. Signals are fed from the top to the bottom. Each channel includes two amplifiers, two discriminators, a delay line and a coincidence.*

After passing through the input protection diode, the analog signal from the straw chamber is input into two amplifiers. The amplifiers serve two purposes:

1) amplify the signal from the chamber. The gain is not easy to determine as it is somewhat related to the size, shape and bandwidth of the input signal. The gain appears to be approximately 10 to 12.

2) shape it to a convenient form for further processing.

Then, the analog signal is divided into two identical parts: one goes into the high threshold discriminator; the other one goes into the low threshold discriminator. The logical signal from the high threshold discriminator is then fed into the coincidence, while the logical signal from the low threshold discriminator is delayed about 5 ns before being fed into a coincidence. Fig. 3.10 shows how the new electronics work. Thus, time walk can be minimized by the low threshold which determines the start time of the signal, while cross talk is removed by the high threshold.

3.3.2 High threshold

Since with the additional amplifier the signal amplitude is increased by at least a factor of 10 and the cross talk amplitude is also increased proportionally. An appropriate threshold value needs to be determined to suppress cross talk.

Bench tests using a ^{106}Ru shown in Fig. 3.11 and an ^{55}Fe[9] sources were done and results are shown in Fig. 3.12. The cross talk count rate, e.g. for the ^{106}Ru source, is described using the scintillator and the ith tube as a trigger to investigate the cross talk in neighbor tube[10].

The left graph in Fig. 3.12 is for the ^{106}Ru source. The source was put on the ith

[9] The basic setup is the same as with the ^{106}Ru source, except there is no scintillator trigger.

[10]

$$Rate = (W_i \cdot Scin \cdot W_{i+1})/(Scin \cdot W_i). \tag{3.4}$$

where 'W_i' and '$W_(i+1)$' represents the hits on tube i and tube (i+1) respectively, and 'Scin' represents the hits on the scintillator.

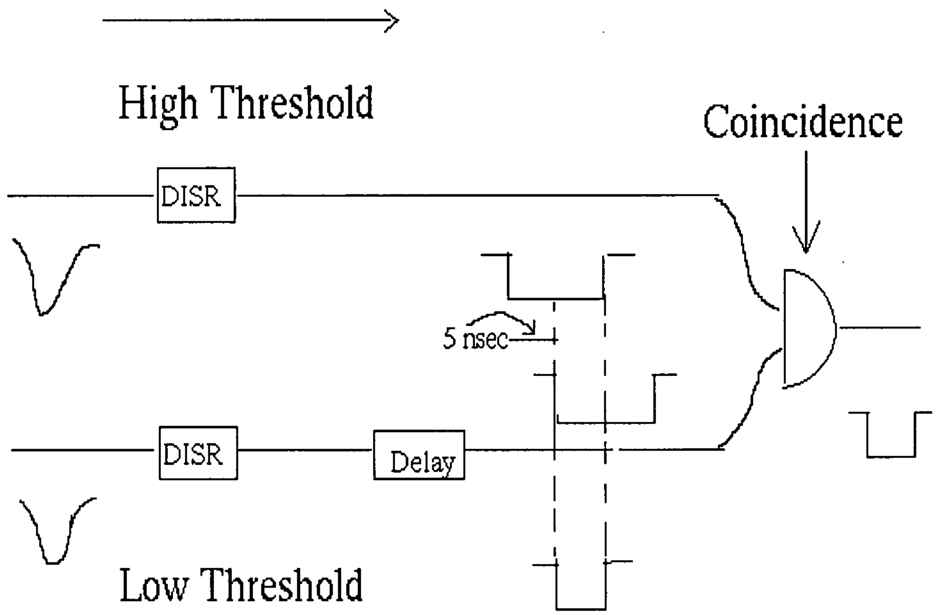

Figure 3.10: *The logic diagram of the dual thresholds of the new electronics. The low threshold is used to determine the start time of the signal, while the high threshold is used to suppress cross talk.*

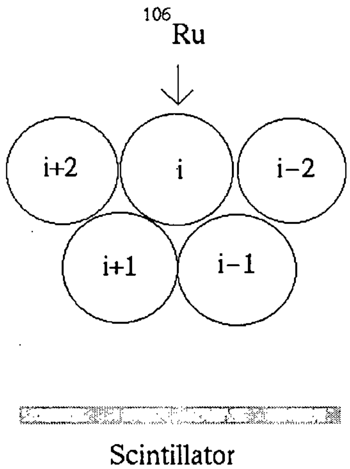

Figure 3.11: *Bench test setup.*

tube. Most of cross talk was removed when the high thresholds were set at > 60 mV. The circles show cross talk induced into a neighbor tube laying in a different sublayer of the RSSC. The rate did not drop down to zero since a particle usually hits two adjacent tubes in different sublayers simultaneously. The triangles show cross talk in a neighbor tube in the same sublayer of the RSSC. The rate was almost down to zero above 60 mV since a particle can't hit two adjacent tubes in the same sublayer simultaneously.

The right graph in Fig. 3.12 was obtained using the ^{55}Fe source to observe the pure cross talk effect. For the ^{55}Fe source, only one tube is hit per event. Thus, when measuring cross talk rate by using an adjacent tube as a trigger, only cross talk induced from that trigger wire is present. When the high threshold was above 60 mV, almost all of the cross talk was removed. Thus, the rate shown in the right graph went down to zero above 60 mV.

It appears that a 60 mV high threshold is suitable to suppress cross talk for all cases.

3.3.3 Low threshold

The function of the low threshold is to minimize time walk. This is illustrated in Table. 3.4 which shows the z resolutions for the upstream, middle and the downstream ends with low threshold at 10 mV and 20 mV, respectively. High thresholds were set at 100 mV enough to suppress cross talk. It is clear that the case of 10 mV low threshold gave a better resolution due to smaller time walk.

3.3.4 Efficiency

The tube fired efficiency is defined as the number of events with the tube and the scintillator[11] fired simultaneously, divided by the number events with only the scin-

[11] The scintillator serves as a trigger.

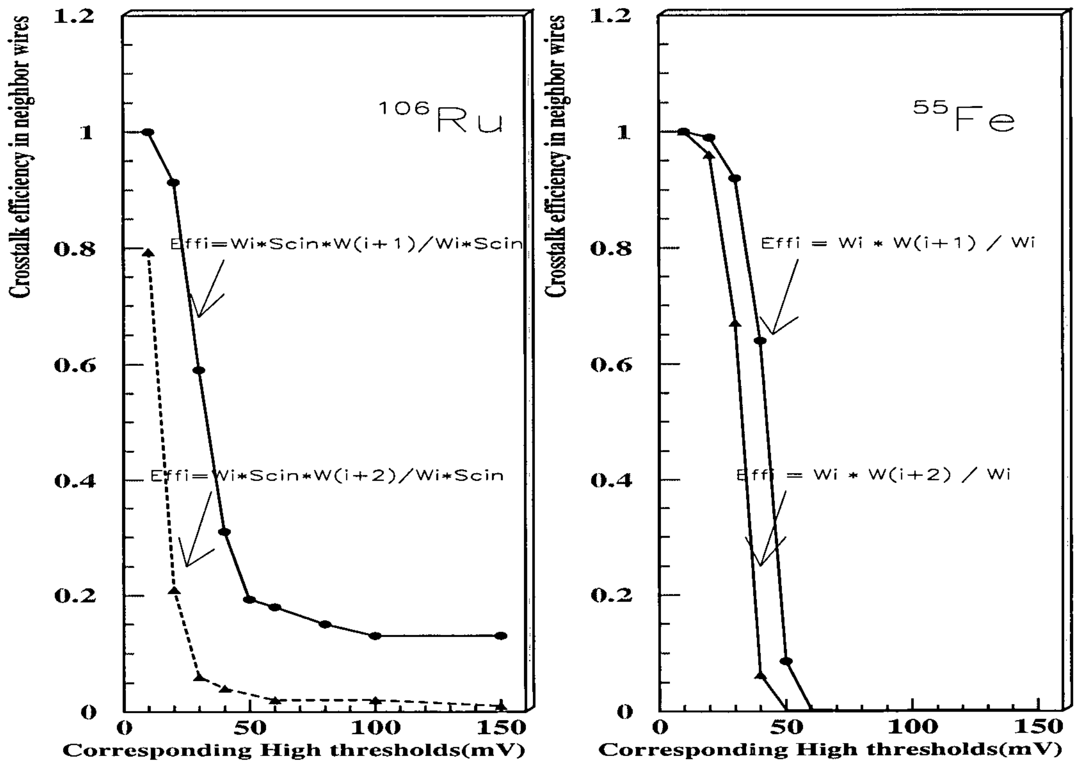

Figure 3.12: *Cross talk count rates in neighbors vs high thresholds of neighbors. The left one is for ^{106}Ru and the right one is for ^{55}Fe. The curves labeled by the circles correspond to the situation that the tubes lay in the different sublayers of the RSSC, while those labeled by triangles correspond to the situation that the tubes lay in the same sublayer of the RSSC, where 'W_i' and '$W_(i+1)$' represents the hits on tube i and tube (i+1) respectively, and 'Scin' represents the hits on the scintillator.*

Low threshold	Upstream	middle	Downstream
10 mV	1.50	1.72	2.36
20 mV	1.77	3.02	3.61

Table 3.4: *Z resolution comparison between different low thresholds on upstream, middle and downstream positions. The lowest threshold gave the best resolution.*

tillator fired[12]. The efficiency depends on the source position and the scintillator position for a given high voltage and a given gas mixture.

Tube 3 and its partner tube 15 were tested on an RSSC chamber. The ^{106}Ru source was on tube 3. The initial decreasing parts suggest that cross talk was removed when the corresponding high thresholds were raised. Above 60 mV, the curves became roughly flat indicating most of the cross talk was removed and the efficiency was roughly 60%. The efficiency of tube 15, kept decreasing above 60 mV. This is because when the true hits occurred on tube 3, signals traveled a longer distance from tube 3 to tube 15 and the signal amplitudes were decreased due to attenuation and dispersion, leading to efficiency loss even with the threshold above 60 mV.

[12] For example,

$$Efficiency = (W_3 \cdot Scin)/(Scin) \tag{3.5}$$

where 'W_3' represents the hits on tube 3 and 'Scin' represents the hits on the scintillator.

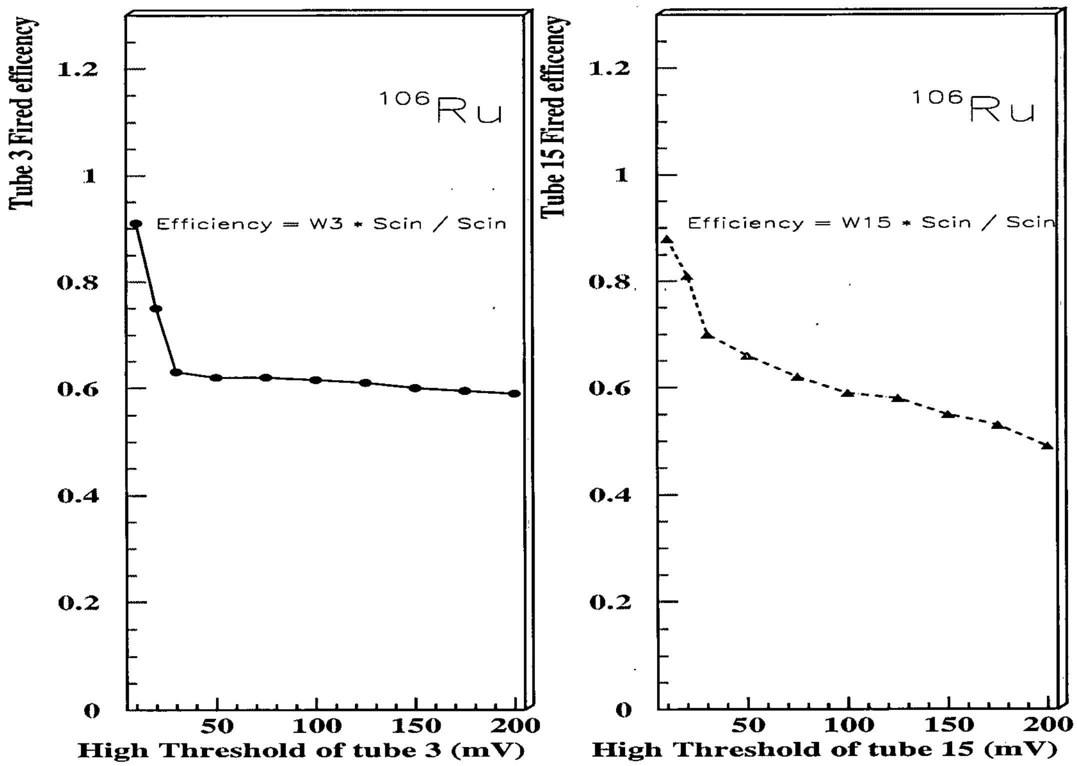

Figure 3.13: *Efficiencies of tube 3 and its partner tube 15. The* ^{106}*Ru source was on tube 3.*

Comparative tests

Comparative tests with/without the add-on board were done to demonstrate how the new board improves the RSSC position resolution.

4.1 Electronics circuit for comparative tests

Let's review the electronics circuits stated in previous chapters. When a hit occurs, two signals are created, corresponding to the leading edge and trailing edge times. Both are fed into separate channels on the new add-on board to remove the cross talk and minimize time walk. Then, the qualified signals from this pair of straws are fed into the external electronics board, where the z information is encoded in an output pulse width (see description of "external electronics"). In E949, the width is measured by subtracting the leading edge time from the trailing edge time using a Fast-bus TDC. To obtain the same information in our bench tests, we used CAMAC TDCs (LRS) and the following system. The signal width was measured by feeding it into logic FAN OUT where it is divided into two parts – one of which is inverted. Then, both are fed into discriminators. Since we use the leading edge of the signal as the discriminator trigger, there is a time difference from these two signals after the discriminators, corresponding to the time difference from the leading and trailing edges of the output signals (see Fig. 4.1). Finally, the z position can be determined from the time difference (as in equation 2.7). Here, the scintillator is used as a trigger to start the TDC when using the ^{106}Ru source.

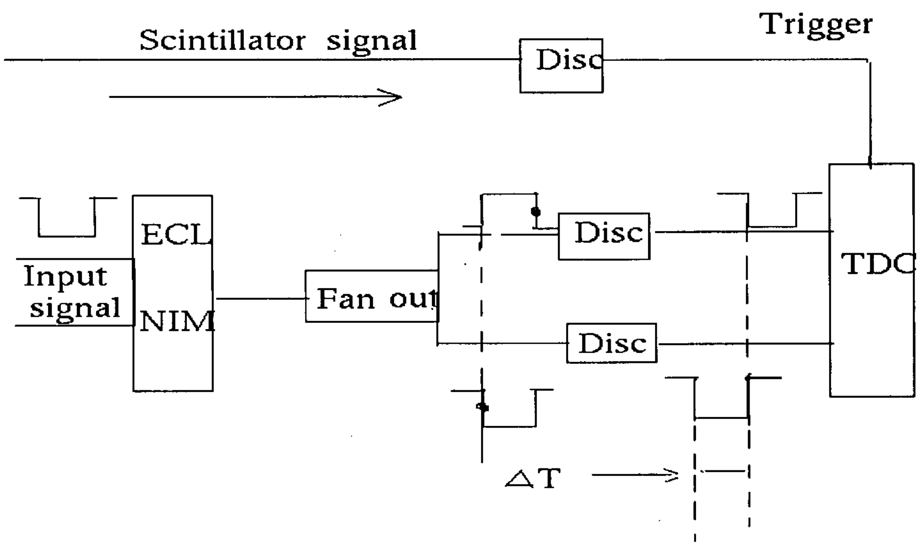

Figure 4.1: *Logic circuit for the bench test of the end-to-end timing measurement.*

4.2 Tests of an inner RSSC

The first tests used an inner RSSC ('S27'). Tube 2 was selected for testing. The test conditions included: 1) the ^{106}Ru source; 2) high voltage at 3450 V and 3) Argon/Isobutane: 25%:75%. The tests were done on the downstream end and the upstream end with/without the new electronics, respectively.

Results in table 4.1 show that the position resolution improvement was correlated with the source position. A factor of 2 (1.3) improvement in resolution was observed on the downstream (upstream) ends.

4.2.1 Selection of the earliest hit tube

In E787, we obtained the z information from the weighted average z of the individual hits in a cluster. In E949, the earliest hit in a cluster is selected as the true hit and its z is used as the z measurement.

In Fig. 4.2 shows the relationship between the tube 2 time and the leading edge

position	σ With add-on board (cm)			σ without add-on board (cm)		
z=	W_1	W_2	W_3	W_1	W_2	W_3
40.5 cm	2.33	1.82	2.33	3.88	5.81	4.69
2.0 cm	2.27	1.79	1.91	2.58	2.78	3.09
-40.5 cm	1.91	1.58	1.94	2.67	2.09	2.33

Table 4.1: *Z resolution comparison for an inner RSSC with/without the add-on board. The ^{106}Ru source was on tube 2 (W_2). The resolutions for W_1, W_2 and W_3 were improved significantly. W_1 indicates tube 1; W_2 indicates tube 2; W_3 indicates tube 3.*

time[1] difference between tube 2 and its neighbors. It is evident that tube 2 gives better time resolution when it precedes its neighbors. Normally, charged particles hit two tubes simultaneously (one in each sublayer of the RSSC). Because the ionization positions are different, the drift distance of the ionizated electrons are different in the two tubes. Thus, the time of arrival at the anodes is different. If the two simultaneously hits arriving within the add-on board coincidence time window[2]. Cross talk from the fast pulse into the other is unavoidable since it superimposes on the signal after which the high threshold is crossed. Thus, averaging the z position from the two simultaneous hits worsens the resolution. The earliest hit in a cluster can be selected to suppress cross talk occurred within the add-on board coincidence time window. The results after this selection are shown in the second column in table 4.2.

Distributions comparison with and without the new electronics is shown in Fig. 4.3. The right graphs are for the cases without the new electronics[3]. while those on the left are for the cases with the new electronics after the earliest hit selection[4]. It is evident that the new electronics is helpful for the resolution improvement and much clean tails can be obtained.

[1] In practice, the leading edge times are used as the hit times.

[2] This time window is determined by the high and the low thresholds shown in Fig. 3.10, approximately 5 ns

[3] The threshold was at 10 mV.

[4] The high threshold was at 60 mV and the low threshold was at 10 mV.

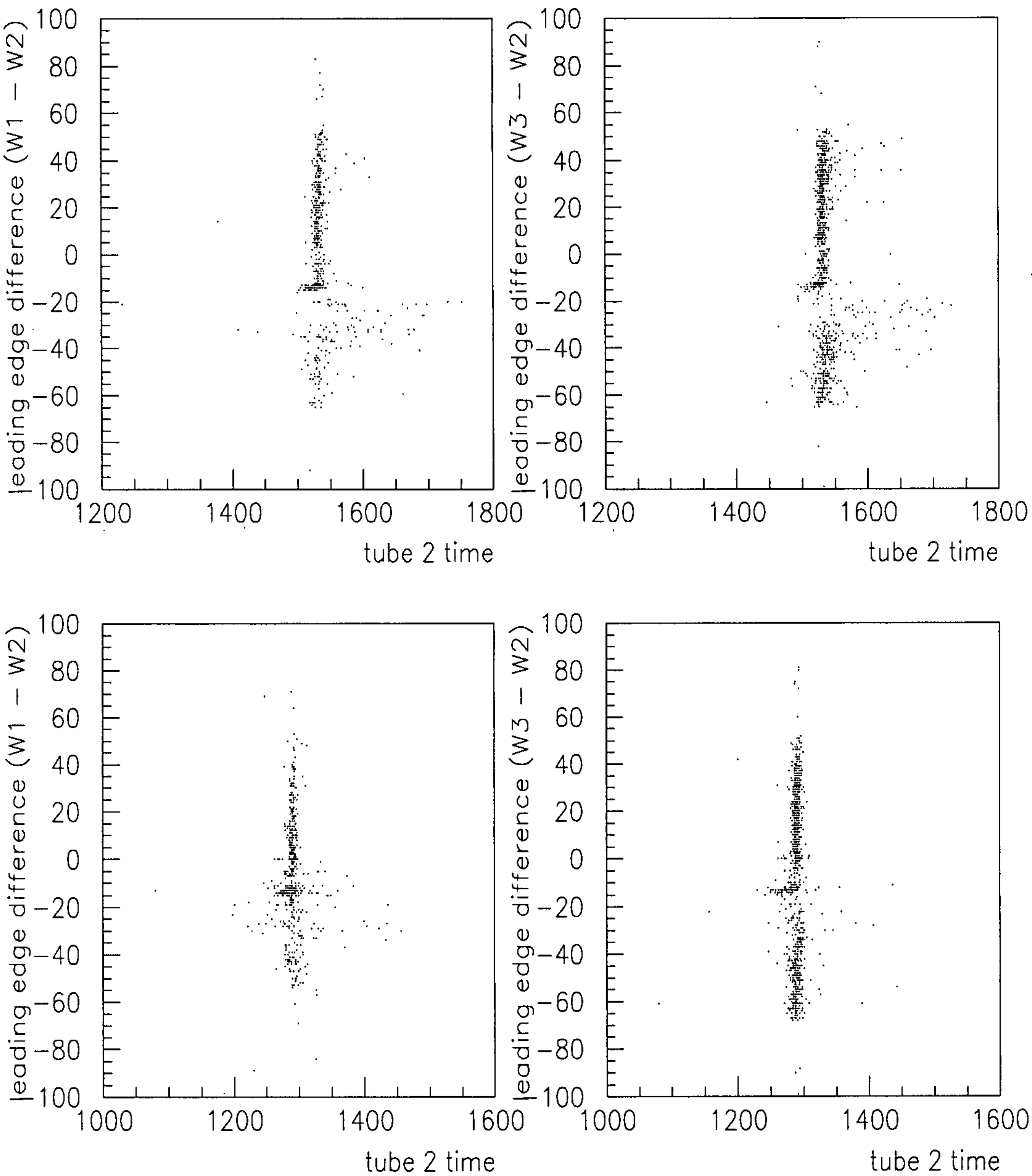

Figure 4.2: *Leading edge time differences vs tube 2 time. The top row graphs are for the downstream end, while the bottom row graphs are for the upstream end. The left two are for cases related to tube 1 and tube 2; while the right two are for cases related to tube 3 and tube 2. It is evident that tube 2 gives better time resolution when it precedes its neighbors.*

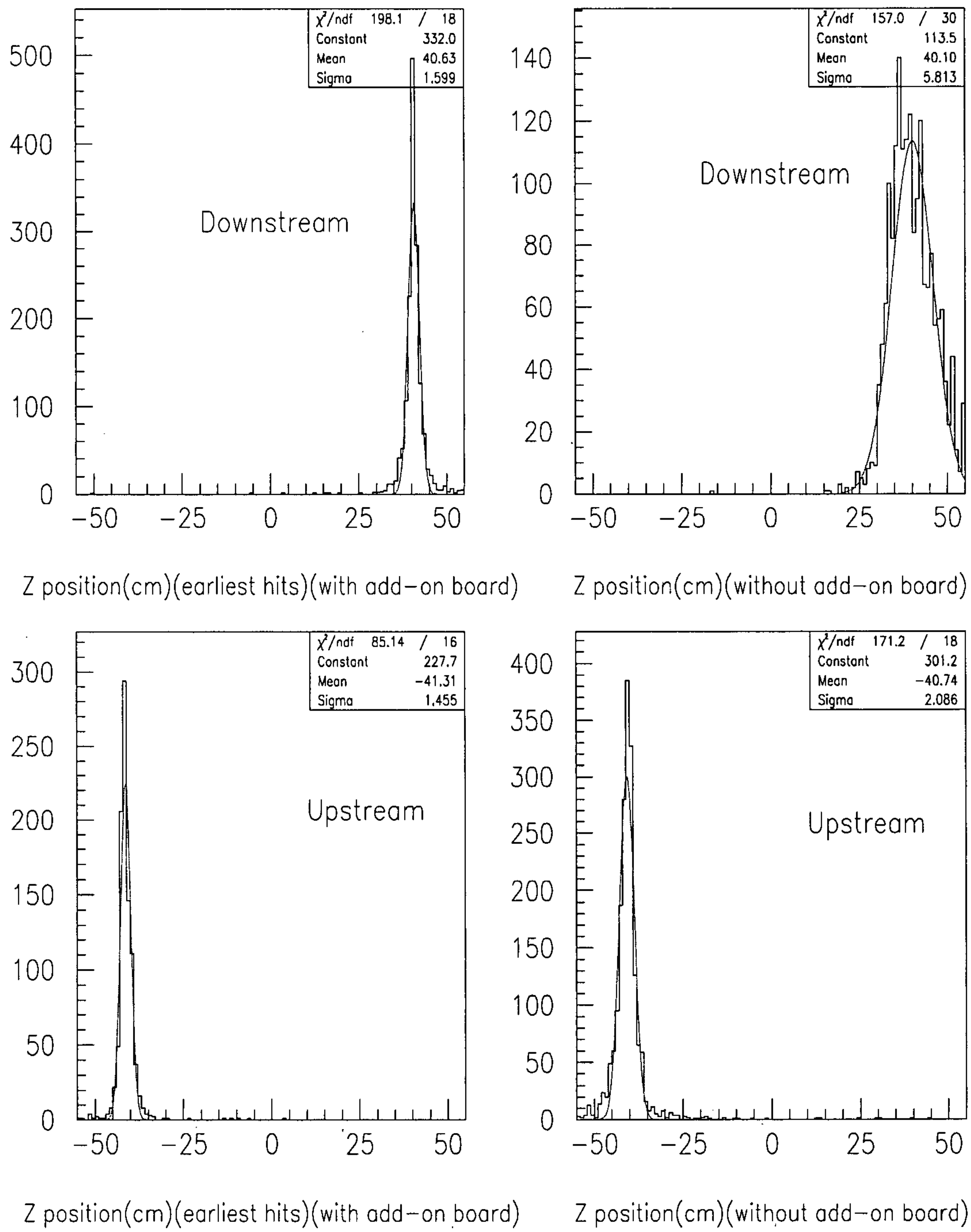

Figure 4.3: *Z information for an inner RSSC with/without the new electronics. The source* ^{106}Ru *was on tube 2. Graphs on the left are for cases with the new board (the earliest hit selection was applied), while those on the right are for cases without the new board.*

position	σ with board (cm)			σ without board (cm)
	'all'	'earliest'	'single'	
40.5 cm	1.82	1.60	1.31	5.81
2.0 cm	1.79	1.55	1.33	2.78
-40.5 cm	1.58	1.46	1.33	2.09

Table 4.2: *Z resolutions of the tube 2 comparison from averages of all hits, the selection of the earliest hits and the single tube hits in an inner RSSC with the new electronics. The results from cases without the new electronics are also listed. "All" means the average time for all hits per cluster, "earliest" means the earliest time among a cluster and "single" means such kind of events with only one tube fired.*

4.2.2 Other contributions to the position resolution

Cross talk is expected to be suppressed when high threshold is set at 60 mV. However, when cross talk comes in on the leading edge of a true hit pulse, as in Fig. 4.4, it will affect the time resolution due to time walk because the timing is determined by the small cross talk pulse and the high threshold is passed by the true hit pulse. The phenomena can be demonstrated by selecting single-tube hits[5]. Results of single-tube hits are shown in Table 4.2. Since cross talk doesn't occur, the resolution from the single-tube hit events is better than the average from all-hit events, even when the earliest hits per event are selected. Unfortunately, we can not exclude this kind of cross talk with the present technique.

4.3 Tests of an outer RSSC

Another comparative tests used an outer straw chamber ('L40A'). The experimental conditions were similar to those for the smaller inner chamber test. The ^{106}Ru source was put on tube 3. In Fig. 4.5, the z peaks with the new electronics on the upstream and the downstream ends show the evident resolution improvement and smaller tail,

[5] A single-tube hit indicates that only one tube is hit per event. Thus, no cross talk occurs at all.

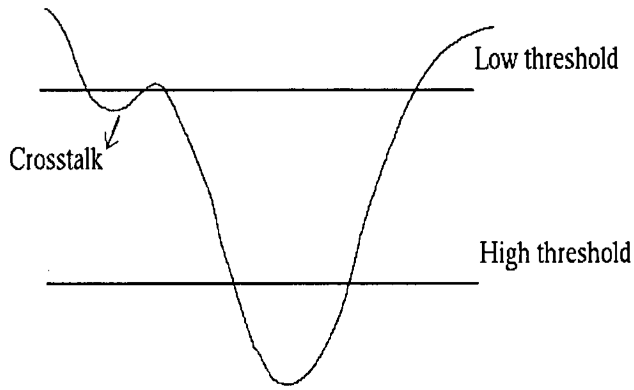

Figure 4.4: *Schematic diagram of the cross talk superimposed on signal, resulting in the time shift.*

Z position	σ with add-on board (cm)			σ without add-on board (cm)		
	W_2	W_3	W_4	W_2	W_3	W_4
37.0 cm	2.67	2.24	2.45	4.09	3.95	3.67
18.5 cm	2.67	1.79	2.49	3.33	3.18	3.58
3.0 cm	2.48	1.61	2.24	3.52	3.03	2.76
-27.5 cm	2.33	1.91	2.06	3.33	3.45	2.46
-46.0 cm	2.24	1.67	2.21	3.09	2.60	2.85

Table 4.3: *Z resolution comparison for an outer RSSC with/without the add-on board. The ^{106}Ru source was on tube 3 (W_3) of an outer RSSC. The resolutions for tube 2 (W_2), tube 3 (W_3) and tube 4 (W_4) were improved using add-on board.*

compared with the cases without the new electronics.

Resolutions with/without the new electronics are listed in Table 4.3. Comparative results among the average of all hits, the selection of the earliest hits and single tube hits are listed in Table 4.4. From these two tables, the same conclusions as for the inner RSSC case are obtained: significant z resolution improvements were achieved using the new add-on board and selecting the earliest hit in a cluster.

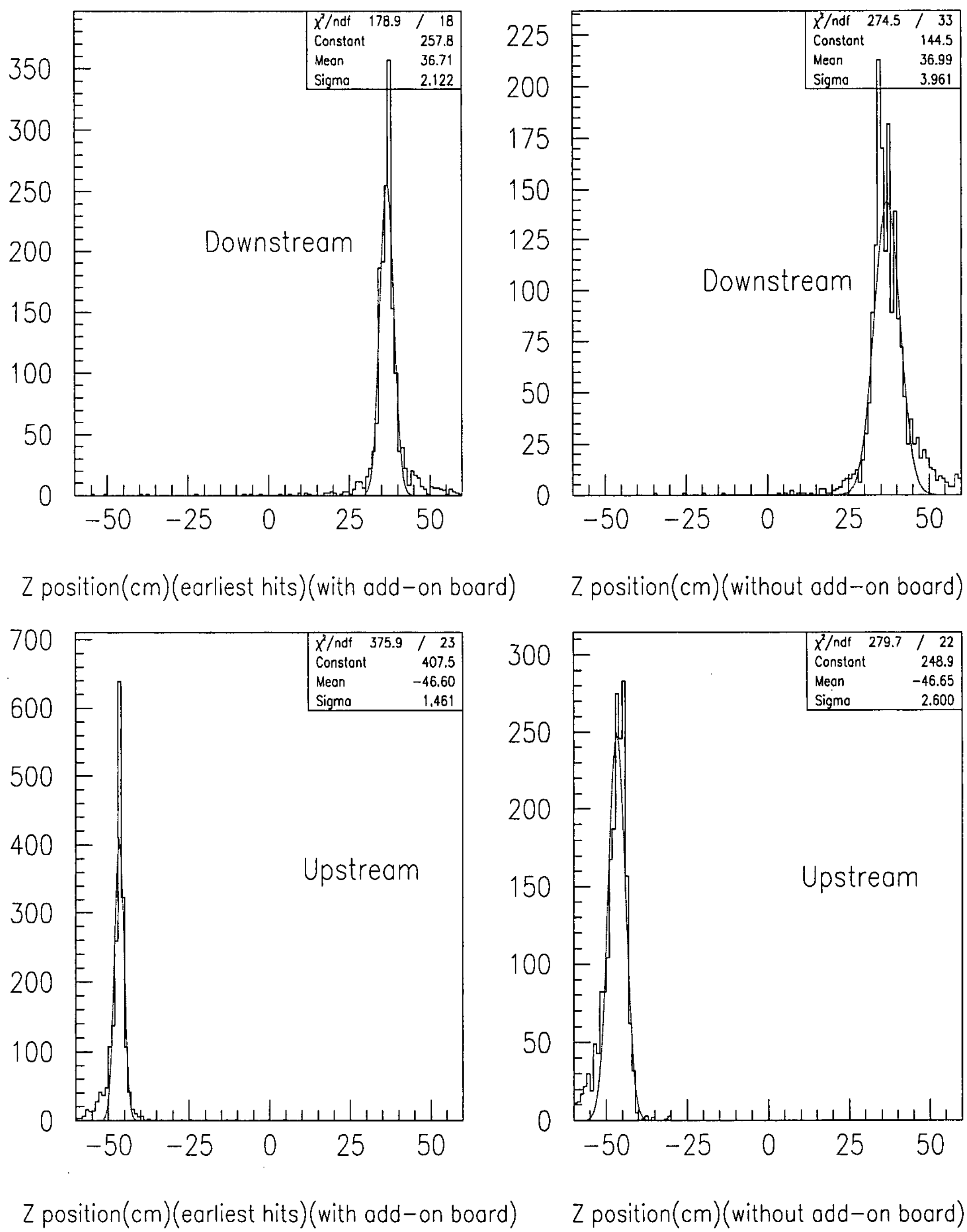

Figure 4.5: *Z information for an outer RSSC with/without the new electronics. The ^{106}Ru source was on tube 3. Graphs on the left are for cases with the new board, while those on the right are for cases without the new board.*

position	σ with board (cm) 'all'	'earliest'	'single'	σ without board (cm)
37.0 cm	2.24	2.12	1.91	3.95
18.5 cm	1.79	1.61	1.30	3.18
3.0 cm	1.61	1.45	1.27	3.03
-27.5 cm	1.91	1.73	1.36	3.45
-46.0 cm	1.67	1.46	1.33	2.60

Table 4.4: *Z resolution comparison of tube 3 from the averages of all hits, the selection of the earliest hits and the single hits in an outer RSSC with the new add-on board. The results from cases without the add-on board are listed also. "All" means the average time for all hits per cluster, "earliest" means the earliest time among a cluster and "single" means such kind of events with only one tube fired.*

4.4 Tests of a production-model electronics

A production-model electronics board with 56 channels was also tested. Two positions on the 'S27A' RSSC were tested on the downstream end (z = 30.25 cm) and the upstream end (z = -38.25 cm). The ^{106}Ru source was moved from tube 1 to tube 12 at each position.

Fig 4.6 shows the z resolutions found with the production board. Run number 1 indicates that the ^{106}Ru source was put on tube 1, and so on. After selecting the earliest hit in a cluster, the typical resolution was about 1.5 cm.

One of the most important issues is the tail of the resolution function. Table 4.5 shows the tail percentages for cases with the new electronics in two positions. Table 4.6 shows the tail percentages for cases without the new electronics in different positions. The main peak percentage was counted in a region ±5 cm around the mean position, while "up-tail" means the tail on the left of the main peak and "down-tail" means the tail on the right of the main peak. Compared table 4.5 with table 4.6, one can conclude that tails are much cleaner in cases with the new electronics. A typical z distribution with the new electronics is shown in Fig. 4.7. The tails are only a few percent of the total.

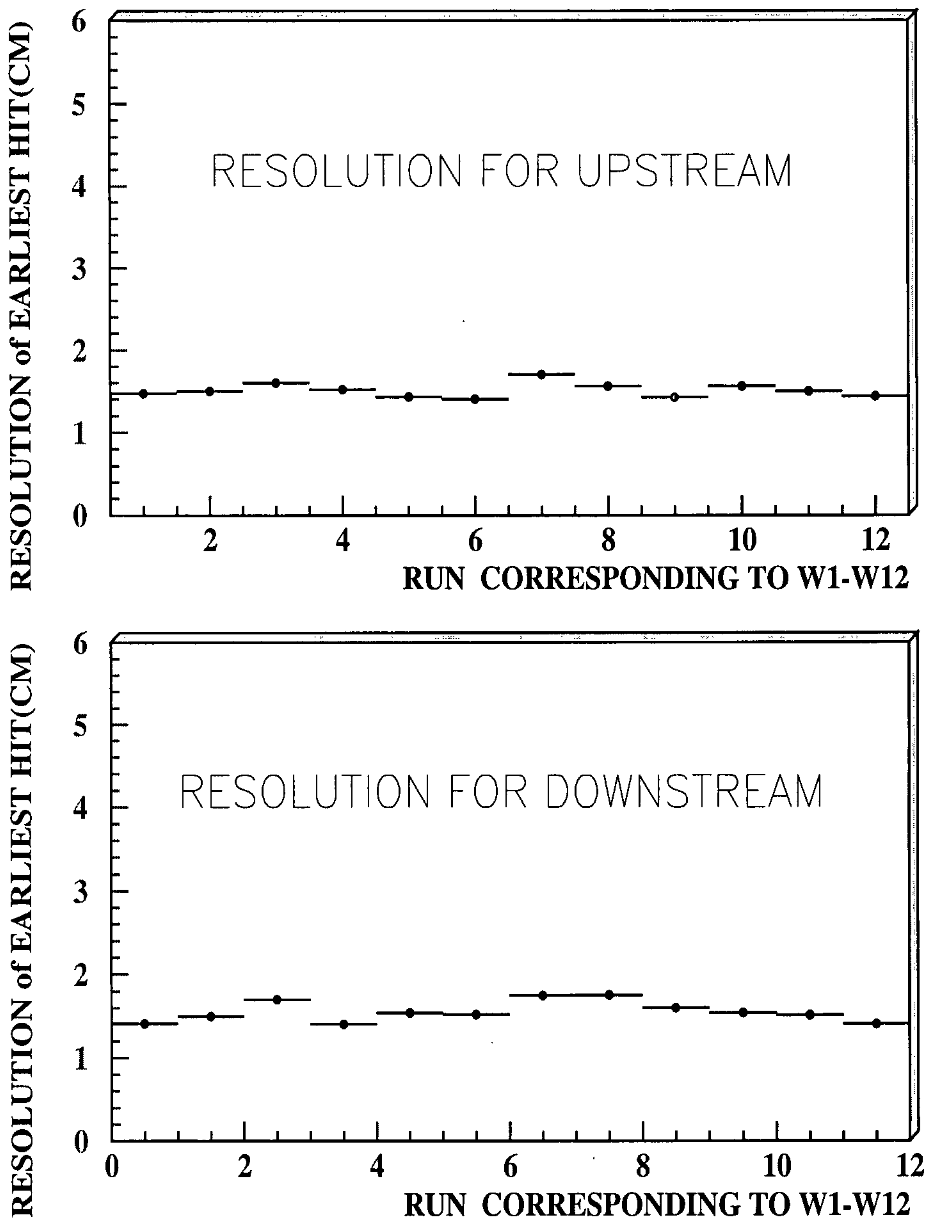

Figure 4.6: *Z resolution (RMS) vs run/tube number on the upstream and the downstream positions when the new electronics was updated to be able to read 56 channels (earliest hits selection was applied).*

Source	Upstream(%)			Downstream(%)		
W_1-W_{12}	up-tl	main	dw-tl	up-tl	main	dw-tl
W_1	2.59	94.83	2.59	4.35	92.44	3.21
W_2	3.11	94.32	2.57	4.07	92.51	3.42
W_3	3.66	92.49	3.85	4.15	91.93	3.92
W_4	4.17	93.63	2.20	4.10	93.68	2.22
W_5	6.01	91.47	2.52	5.17	90.50	4.54
W_6	3.97	93.28	2.76	4.12	92.93	2.96
W_7	3.24	93.04	3.72	6.95	87.70	5.33
W_8	3.12	93.18	3.65	6.98	89.50	3.53
W_9	3.95	91.69	4.36	4.47	91.36	4.17
W_{10}	1.70	95.65	2.60	1.90	94.15	3.94
W_{11}	3.25	92.47	4.28	2.84	93.30	3.86
W_{12}	2.75	92.23	5.02	4.30	92.22	3.48

Table 4.5: *Percentages of up-tail (up-tl), main peak and down-tail (dw-tl) in two positions for an RSSC with the new electronics*

position (cm)	up-tl	main	dw-tl (%)
36.5	5.43	87.73	6.84
19.5	5.52	87.15	7.33
-6.5	5.01	88.07	6.92
-32.0	4.93	88.14	6.93

Table 4.6: *Percentages of up-tail (up-tl), main peak and down-tail (dw-tl) in different positions for an RSSC without the new electronics.*

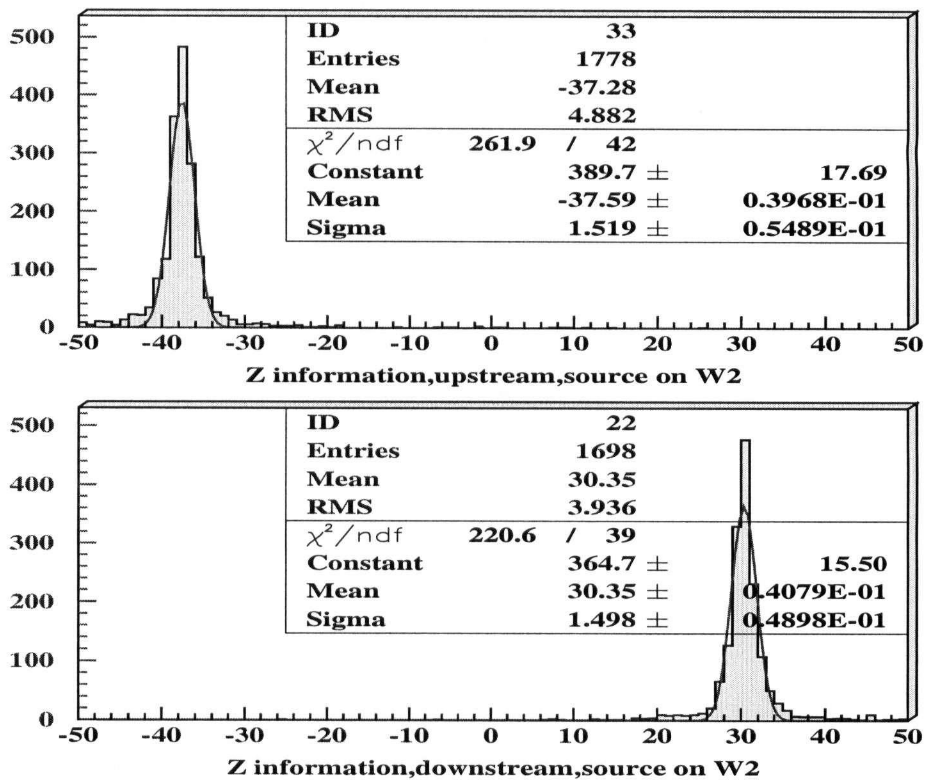

Figure 4.7: *Position measurements when the source was on tube 2 on the upstream and downstream ends, respectively. The earliest-hit selection was applied.*

The RSSC in E949 experiment

5.1 Overview

The new experiment E949 has many improvements to the E787 apparatus and to the Alternating Gradient Synchrotron operation mode. It is expected to reach a sensitivity of (8-15)$\times 10^{-12}$, an order of magnitude below the SM prediction[20] for $K^+ \to \pi^+ \nu\bar{\nu}$. This will result in a determination of $|V_{td}|$ to be better than 30%. The increased sensitivity of E949 is achieved by a combination of several factors, such as an increased number of protons per AGS spill on the kaon production target, detector improvements, improvements to the data acquisition system, and longer running periods. The RSSCs upgraded with add-on electronics boards were installed in E949 in November 2001.

5.2 RSSC calibration

RSSC calibration includes the t_0 calibration, the calibration of the effective tube velocities and the chamber lengths and the calibration of the middle point times.

5.2.1 The t_0 calibration

Since signals from different straw pairs are fed into different external electronic channels, the travel time in the cables and electronic channels may be different due to the different cable lengths, hardware response times, etc. The leading edge time is used as the time of the hit. Fig. 5.1 shows two tubes' leading edge times from $K_{\mu 2}$ data. The distributions start at different places which indicates that the external travel times depend on the electronic channels. In practice, fitting the initial steep cliff of the leading edge time gives a value t_0. Then applying formula 5.1 to the leading edge time

$$t_{leading(cali)} = |t_0| - t_{leading} \tag{5.1}$$

moves the leading edge time to start at zero. Thus, the impact from the different performance in each electronic channel is suppressed.

In the improved RSSC system, the t_0 calibration becomes important since the earliest leading edge times are treated as the true hit times and correctly selecting them is helpful to minimize time walk. A data set of at least 10^6 $K_{\mu 2}$ events is used to do the t_0 calibration.

5.2.2 The effective chamber lengths, velocities and the middle point times calibration

Time information from the TDC is converted into z information using equation 5.2 (same as Equ. 2.7):

$$z = K\Delta t + B, \tag{5.2}$$

where K is the effective velocity and B is the effective chamber length of the straw tube as discussed in Section 2.3.2. Δt is the time difference between the trailing and leading edge times:

$$\Delta t = t_{trailing} - t_{leading}{}^{1}. \tag{5.3}$$

A sample of 10^7 ^{55}Fe data is used for this calibration and for diagnostics. ^{55}Fe sources are deposited on mylar strips, which are glued across the outside of the

[1] Since the trailing edge and leading edge times share the same external electronic channel, t_0 should be the same and be canceled in Equ. 5.3.

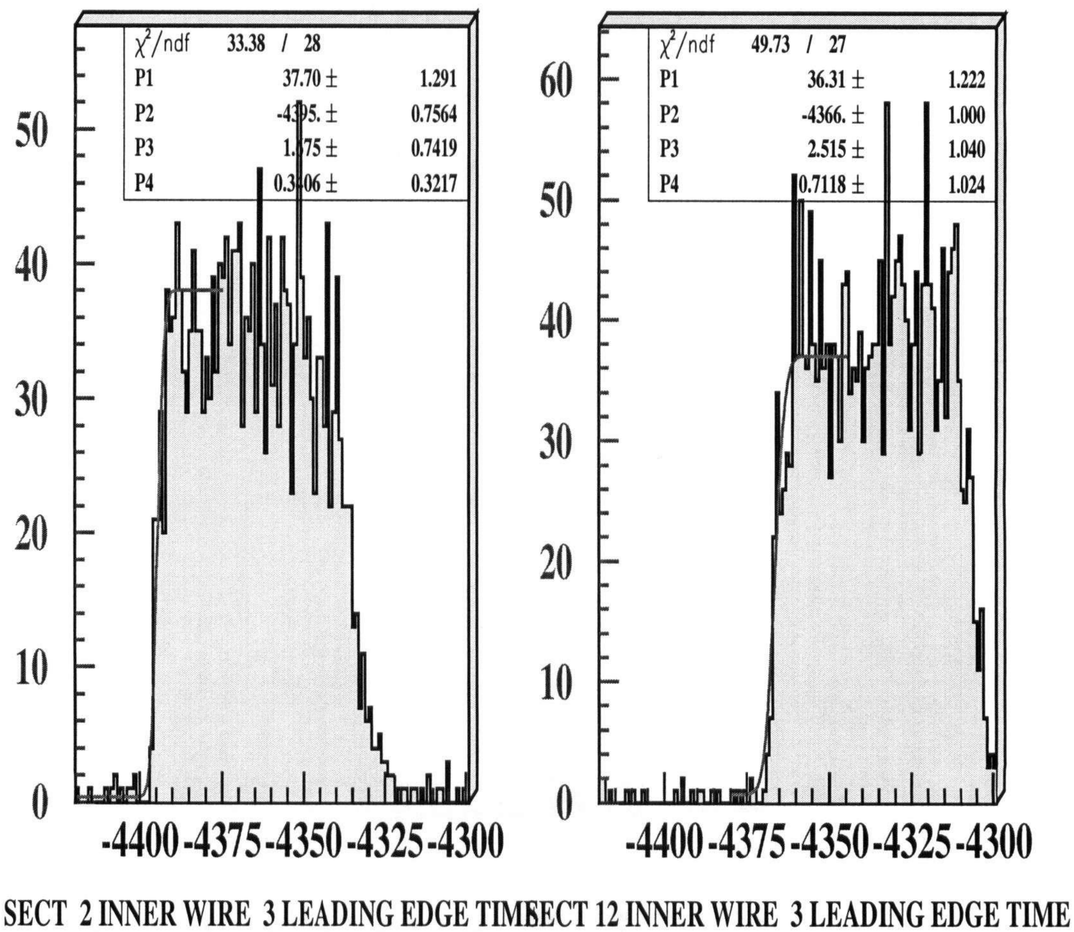

Figure 5.1: *The leading edge time shift from two different channels indicates the necessity to do the* t_0 *calibration.*

straw chamber. Two strips are glued on the upstream and the downstream surfaces at constant z positions. Each straw tube therefore has two ^{55}Fe induced peaks, and each electronic channel (a straw pair) has four, shown in the bottom graph in Fig. 5.2. The first and fourth peaks correspond to the same position on the downstream end, while the second and third ones correspond to the same position on the upstream end.

The calibration procedures are :

- Using the two known position difference divided by their time difference to get the effective velocity. The following formula depicts how to get the effective velocity and chamber length for a late tube[2], where z_1, z_2 and Δt_1, Δt_2 correspond to the first two peaks z positions and times.

$$z_1 = K_{late}\Delta t_1 + B_{late} \tag{5.4}$$

and

$$z_2 = K_{late}\Delta t_2 + B_{late} \tag{5.5}$$

The effective velocity can be obtained by the subtraction of above two formula:

$$K_{late} = \Delta z_{12}/\Delta t_{12}. \tag{5.6}$$

where Δz_{12} = (z_1 - z_2) and Δt_{12} = (Δt_1 - Δt_2).

- Then, the effective length for that tube can be computed by either

$$B_{late} = z_1 - K_{late}\Delta t_1 \tag{5.7}$$

[2] Recall that one of the pair tubes is called the early tube and the other one is called the late tube since the signals from the former always come earlier that those from the latter due to the 25 nsec passive delay line of the latter. The first and second peaks in Fig. 5.2 correspond to hits occurred on the late tube and the third and fourth peaks in Fig. 5.2 correspond to hits occurred on the early tube .

or

$$B_{late} = z_2 - K_{late}\Delta t_2, \tag{5.8}$$

Slopes and intercepts for all channels from ^{55}Fe calibration are plotted in the first row of graphs in Fig. 5.2. Dots scatter evenly around a constant slope and intercept. Since each channel has two tubes, there are two sets of slopes and intercepts for each channel. The positive slope and negative intercept are for hits occurred at the early tube, while the negative slope and positive intercept are for hits occurred at the late tube.

- The middle point[3] (around 1080 ns) is used to determine which tube in a pair is hit. Hit times later than the middle point times indicates that the hits occurred on the early tube, while hit times earlier than the middle point times indicates that the hits occurred on the late tube. Thus, the first two peaks in the bottom graph in Fig. 5.2 corresponds to hits on the late tubes and the last two peaks corresponds to hits on the early tubes. The middle point time can be obtained from previous calibration by subtraction of Equ. 5.10 from Equ. 5.9, where z_{middle} is the middle point z position:

$$z_{middle} = K_{early}\Delta t_{middle} + B_{early}, \tag{5.9}$$

$$z_{middle} = K_{late}\Delta t_{middle} + B_{late}, \tag{5.10}$$

Thus,

$$\Delta t_{middle} = \frac{B_{late} - B_{early}}{K_{late} - K_{early}}, \tag{5.11}$$

where, K_{late} and B_{late} are the effective velocity and length of the late tube and K_{early} and B_{early} are those of the early partner.

[3] This is the connection point of the two straw tubes of a pair in the jumper card.

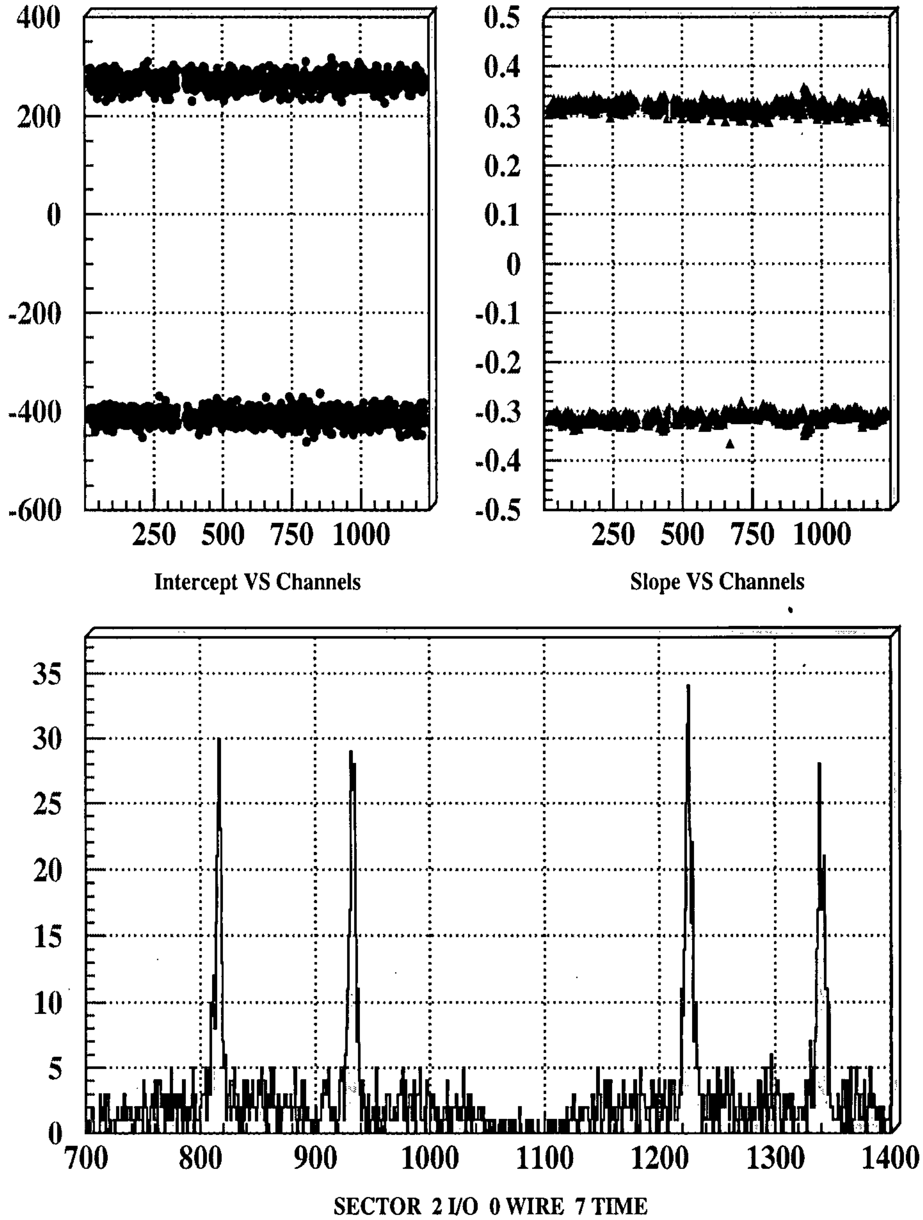

Figure 5.2: *The slopes (effective velocities) and intercepts (effective chamber lengths) calibration using* ^{55}Fe *data in E949. The bottom graph shows the normal four peaks in a channel.*

5.3 Results from E949 RSSC data

From August 2001 to November 2001 , a new electronic system was installed in the sector 18 inner RSSC in E949 to test its performance.

5.3.1 Improved π^+/μ^+ separation

As mentioned in chapter 2, the E787 RSSC z was calculated by a weighted average z of the individual hits in a cluster. In E949, the earliest his selection is applied to choose the true hit in a cluster and that z is treated as the true measurement. The improved residual resolution from the 2001 data will be more helpful to do the off-line muon rejection. Fig. 5.3 shows this idea using 1998 and 2001 $K_{\pi2}$ data[4] and a large angle scattering muon sample. One can conclude that the cut on the residual (Z_{UTC}-Z_{RSSC}) can be tightened due to the better 2001 $K_{\pi2}$ z resolution to reject more scattering muons, while still have a good $K_{\pi2}$ acceptance.

5.3.2 Results from cosmic ray data

High energy cosmic data was used to check the RSSC performance. The results were consistent with the bench tests, as shown in Fig. 5.4. The resolution of sector 18 was 2.2 cm or about 1 cm better than neighboring sectors without the new electronics[5].

5.3.3 Results from $K_{\mu2}$ data

$K_{\mu2}$ data was used to do the same analysis. The data showed that 53% of the events had 2 hits per cluster and 24% of the events had 3 hits per cluster. Among the 2 hits/cluster events, more than 91% of the events had two tubes hit simultaneously.

Some basic cuts were applied, such as requiring 6 hits in the UTC r-z planes, good momentum reconstruction, good individual residuals in the UTC, and good

[4] This is the data from the sector 18 of the inner RSSC with the new electronics

[5] In order to have enough statistics, no earliest selection was used here for the cosmic ray data.

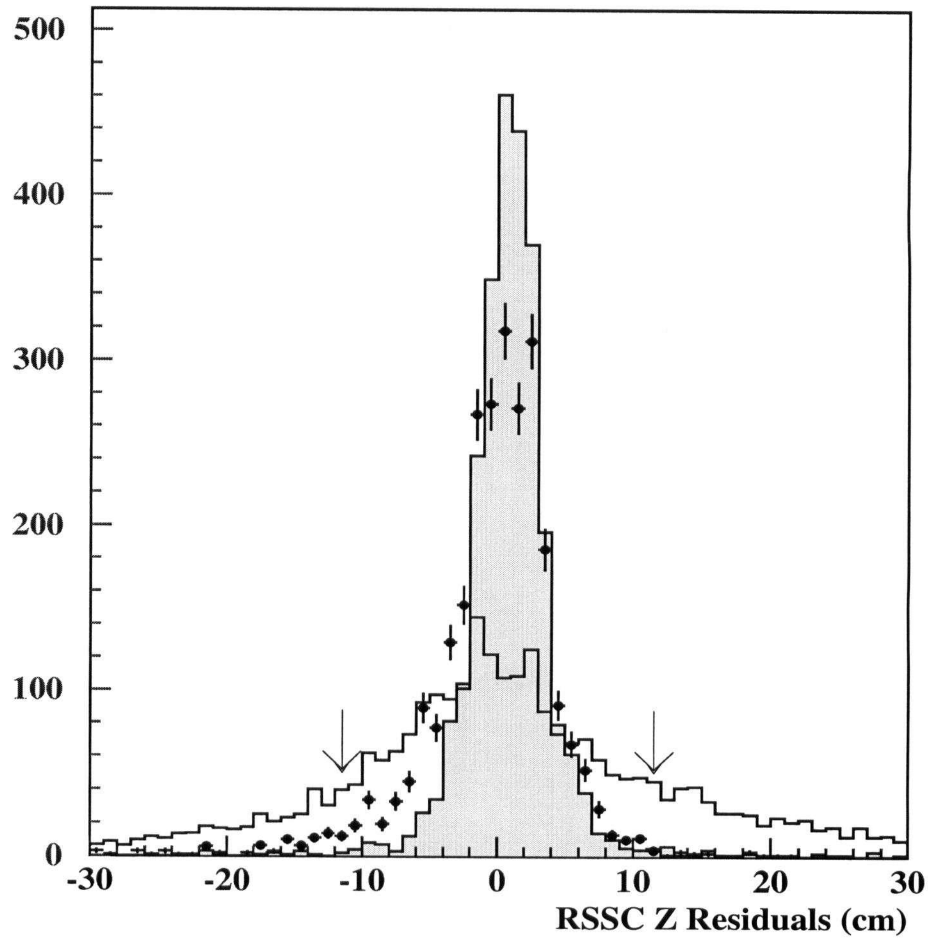

Figure 5.3: *Resolution comparison of $K_{\pi 2}$ sample between 1998 and 2001 data. The narrow and tall peak represents the 2001 result and the dots superimposed on the peak represents the 1998 result. The wide and short peak represents large angle scattering muon sample. In order to separate this kind of background muons from pions, a cut on the RSSC residual can be applied, which is indicated by two arrows in the graph on 1998 data. This cut can be tightened further in 2001 data to obtain larger muon rejection.*

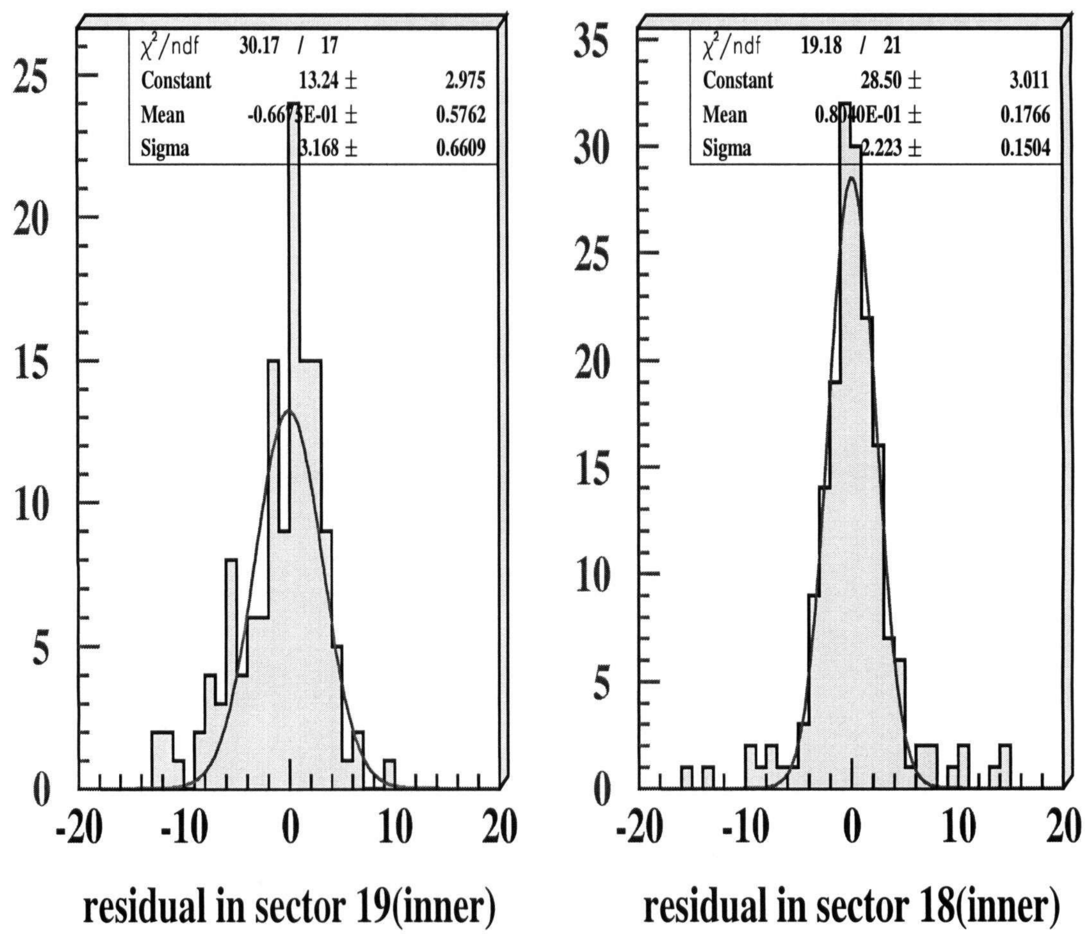

Figure 5.4: *Residual (Z_{utc} - Z_{rssc}) of the cosmic ray data without (left graph) and with (right graph) the new electronics in E949.*

track fitting in order to suppress the uncertainty from the UTC. The results are shown in fig. 5.5.

The measured resolution was 1.8 cm (see Fig. 5.5) and the resolution from the Monte Carlo simulation was 1 cm. Thus, the contribution from the RSSC was approximately 1.5 cm[6], consistent with the bench test results.

5.3.4 Efficiency

The RSSC efficiencies were obtained using RS counters in the same sector as trigger which are located at the inside and outside of the RSSC, i.e., requiring the charged track passing through both RS counters located inside and outside of the RSSC, and checking if the RSSC fired or not. For an inner RSSC, the efficiency is defined as "(layer10 · RSSC · layer11)/(layer10 · layer11)" and for an outer RSSC, it is defined as "(layer14 · RSSC · layer15)/(layer14 · layer15)".

The E949 RSSC efficiencies were measured using the $K_{\mu 2}$ and the π_{scat} data[7]. The average efficiencies for all the inner and outer RSSCs are shown in table 5.1. The efficiency losses in the $K_{\mu 2}$ data, compared to the 1998 data, can be explained as following. The energy losses from muons in the RSSCs are lower than those from pions due to the smaller mass. Thus, the smaller signal amplitudes of muons could lead to the signals from the trailing edge tubes being missed if the current high thresholds are high enough to cut some of them. The worse $K_{\mu 2}$ efficiencies in the inner RSSCs also illustrate that the signal amplitudes have an impact on the efficiency since muons have smaller signal amplitude in the inner RSSC due to the smaller energy losses, leading to some signals were crossed out by the high thresholds. However, muons

[6]
$$\Delta\sigma_{rssc} = \sqrt{\sigma^2_{measured} - \sigma^2_{mc}}. \tag{5.12}$$

[7] For the π_{scat} sample, events are required to be well reconstructed, to be identified as pions, no photons detected, most importantly they should be consistently with beam background.

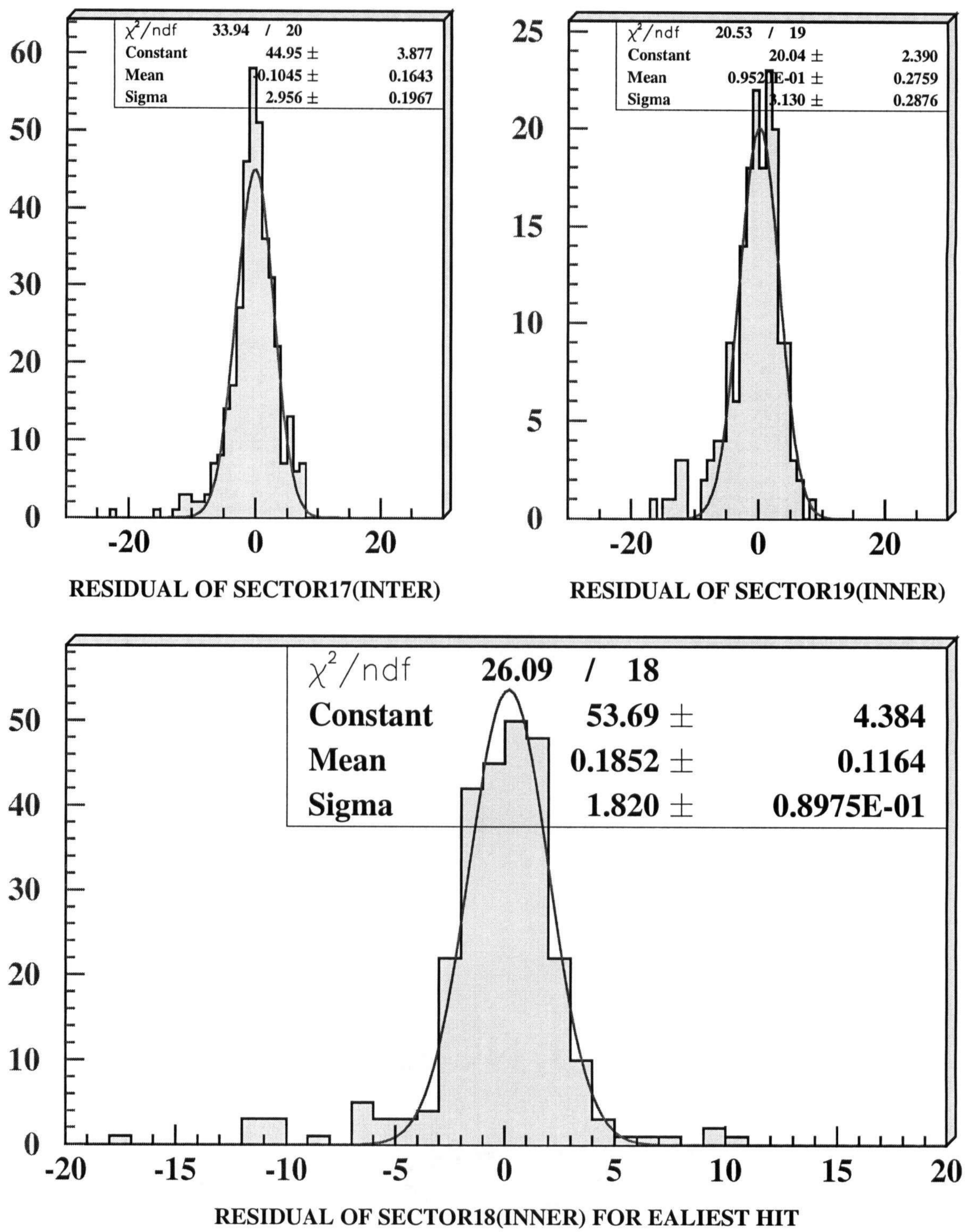

Figure 5.5: *Residuals of (Z_{UTC} - Z_{RSSC}) of the $K_{\mu 2}$ data in sectors 17,18 and 19 in E949. Only sector 18 is equipped with the new electronics for which the resolution is one centimeter better than its neighbors.*

	2002 data		1998 data	
	$K_{\mu 2}$	π_{scat}	$K_{\mu 2}$	π_{scat}
Inner	89.2±1.6	96.1±1.5	99.1±0.08	99.0±0.2
Outer	92.9±1.4	98.1±1.5	99.6±0.07	99.6±0.3

Table 5.1: *The Efficiency comparison for the 1998 and 2002 data.*

are the background of the $K^+ \rightarrow \pi^+\nu\bar{\nu}$ study whose lower efficiency is helpful to do the online suppression. The estimated efficiency errors are much bigger than those in 1998 due to the lower statistics available at present[8].

[8] The error is estimated by the following formula:

$$Error = \sqrt{\frac{P(1-P)}{N}} \tag{5.13}$$

where P is the efficiency and N is the denominator when doing the efficiency calculation.

Conclusion

The poor E787 RSSC z measurement was hypothesized to be due to time walk effects. Due to the special RSSC design that the straws are connected into pairs on the upstream end and read out only from the downstream end, the RSSCs use end-to-end timing to get z information. Different signal amplitudes affect the time measurement and result in poor z resolution.

New electronics add-on boards for the E949 RSSC detectors have been designed and tested at TRIUMF. The signals are amplified and then subjected to two discriminator thresholds per channel. The low threshold is used to minimize time walk and the high one is used to suppress cross talk. The bench tests gave a satisfactory result with a typical z resolution approximately 1.5 cm, an improvement of a factor of 2.

The add-on boards were installed in E949 at BNL. The new RSSC system has provided better z position measurements, compared to the old RSSC system. 2001 $K_{\mu2}$ data showed that the z resolution of the new RSSC system was 1.8 cm, while the original system gave 3 cm. The resolution contribution from multiple-scattering in the MC simulation is 1 cm. Therefore, the contribution from the RSSC can be estimated to be 1.5 cm, consistent with bench test results. The improved z measurements of the RSSCs are expected to give a better π^+/μ^+ separation. In addition, more muon background rejection can be achieved due to the fact that the efficiency of the new system for the muon sample is significantly lower than that for the pion sample.

References

[1] S.Alder *et al., Physical Review Letters, Volume 88, Number 4 (2002)*

[2] Jesse R.Stone, Ph.D thesis, Princeton University (1998)

[3] L. Wolfenstein, Phys. Rev. Lett. **51**, *(1945)*

[4] Douglas Bryman, Techniques and Concepts of High Energy Physics X, 111-145 (1999)

[5] Review of Particle Properties, Phys.Rev.D50, Part 1, (1994)

[6] Robert A.McPherson, Ph.D thesis, Princton University (1995)

*[7] Rein, D., and Sehgal, L.M., Phys. Rev.***D39**, *(1989)*

[8] Paul Bergbusch, Ph.D thesis. University of British Columbia(2001)

[9] M.S. Atiya, E.W.Blackmore, P.C. Bergbusch, D.A. Bryman, S.Chen, etc., E949 technic notes, BNL-67247, 4 (1999)

[10] Frank E.Taylor, Nuclear Instruments and Methods A289(1990)

[11] G. Charpak et al., IEEE Trans. Nucl. Sci. NS-25 (1978) 122.

[12] J. Fisher, Nucl. Instr. and. Meth. 151 (1978) 451.

[13] M. Atac and A.V. Tollestrup, Preprint FN-339, Fermilab (July 10, 1981).

[14] D. Potter, Nuclear Instr and Meth 200 (1982) 345-354

[15] *V.A. Lozanskii and O.B.Firsov, Sov.Phys. JETP 29 (1969) 267.*

[16] *E. Iarocci, Nucl. Instr. and. Meth. 217 (1983) 30-42.*

[17] *G. Battistoni, E. Iarocci, Nucl. Instr. and. Meth. 164 (1979) 57-66.*

[18] *John D. Naud, Technical Note No.333, E787 TN 333 (1997)*

[19] *E949 technic note BNL-67247 tri-pp-00-06*

[20] *A.Buras hep-ex/0109197*